

**UNIVERSIDADE DE BRASÍLIA  
FACULDADE GAMA / FACULDADE DE TECNOLOGIA  
PROGRAMA DE PÓS-GRADUAÇÃO EM INTEGRIDADE DE  
MATERIAIS DA ENGENHARIA**

**NUMERIC SIMULATION OF DEVELOPING TURBULENT FLOW IN  
ECCENTRIC CHANNELS – EFFECT OF THE VELOCITY  
FLUCTUATIONS ON THE CONVECTIVE HEAT TRANSFER**

**DIANA CATERINNE SANDOVAL CANDELA**

**ADVISOR: Dr. Jhon Nero Vaz Goulart**

**DISERTAÇÃO DE MESTRADO EM INTEGRIDADE DOS MATERIAIS  
DA ENGENHARIA**

**PUBLICATION: FGA.DM-080A/2019  
BRASÍLIA/DF: MAI – 2019**

**UNIVERSIDADE DE BRASÍLIA**

**FACULDADE GAMA / FACULDADE DE TECNOLOGIA**

**PROGRAMA DE PÓS-GRADUAÇÃO EM INTEGRIDADE DE  
MATERIAIS DA ENGENHARIA.**

**DIANA CATERINNE SANDOVAL CANDELA**

**NUMERIC SIMULATION OF DEVELOPING TURBULENT FLOW  
IN ECCENTRIC CHANNELS – EFFECT OF THE VELOCITY  
FLUCTUATIONS ON THE CONVECTIVE HEAT TRANSFER**

**DISSERTAÇÃO DE MESTRADO SUBMETIDA AO PROGRAMA DE PÓS-GRADUAÇÃO E INTEGRIDADE DE MATERIAIS DA ENGENHARIA DA FACULDADE GAMA E FACULDADE DE TECNOLOGIA DA UNIVERSIDADE DE BRASÍLIA, COMO PARTE DOS REQUISITOS NECESSÁRIOS PARA OBTENÇÃO DO GRAU DE MESTRE EM INTEGRIDADE DE MATERIAIS DA ENGENHARIA.**

Advisor: Prof. Dr. Jhon Nero VazGoulart

BRASÍLIA

2019.

**UNIVERSIDADE DE BRASÍLIA  
FACULDADE DO GAMA / FACULDADE DE TECNOLOGIA  
PROGRAMA DE PÓS-GRADUAÇÃO EM INTEGRIDADE DE  
MATERIAIS DA ENGENHARIA**

**"NUMERIC SIMULATION OF DEVELOPING TURBULENT FLOW IN AN  
ECCENTRIC CHANNEL - EFFECT OF THE VELOCITY FLUCTUATIONS ON  
THE CONVECTIVE HEAT TRANSFER"**

**DIANA CATERINNE SANDOVAL CANDELA**

**DISSERTAÇÃO DE MESTRADO SUBMETIDA AO PROGRAMA DE PÓS-GRADUAÇÃO  
EM INTEGRIDADE DE MATERIAIS DA ENGENHARIA DA FACULDADE DO GAMA E  
FACULDADE DE TECNOLOGIA DA UNIVERSIDADE DE BRASÍLIA, COMO PARTE DOS  
REQUISITOS NECESSÁRIOS PARA A OBTENÇÃO DO GRAU DE MESTRE EM  
INTEGRIDADE DE MATERIAIS DA ENGENHARIA.**

**APROVADA POR:**



**Prof. Dr. Jhon Nero Vaz Goulart; FGA / UnB  
(Orientador)**



**Prof. Dr. Rodrigo Andres Miranda Cerda; FGA / UnB  
(Membro Interno)**



**Prof. Dr. Luiz Carlos Wrobel; PUC/RJ  
(Membro Externo)**

**Brasília / DF, 24 de maio de 2019**

To my Parents and sister  
For been with me in every step of my life.

## **AKNOWLEDGEMENTS**

To my mom, Luz Mery, my dad, Jose Orlando and sister, Silvia Alexandra for always been to my side in spite of the distance and support every choice I ever made in my life.

To God, for all the awesome people I have met during this amazing journey.

To my Colombian friends and Brazilian family, they have been and important wheel in this process, without your support this would not have been possible.

To Prof. Dr. JhonGoulart, for the trust, the help and the advising during this process.

To CAPES for the financial support.

## ABSTRACT

Forced convection heat transfer and the characteristics of the flow in annulus passages are important phenomena in the engineering field. Many engineering applications have concentric and eccentric annulus pipe flows such as heat exchangers, nuclear reactors, solar energy systems, thermal storage systems, cooling of electronic devices. Some annular passages appear as a result of fabrication or construction errors, leading to tube misalignment and, therefore, the appearance these geometric configurations with very narrow passages. In both cases, it is important to know and understand the behavior of the flow. The new geometry configurations may affect the physics of the heat transfer phenomena for instance.

The aim of this work is to investigate the effect of the velocity fluctuations in the heat transfer coefficients for eccentric channels using numerical simulation. The main geometric parameters of the channel are the length,  $L=1500$  mm and the diameter ratio  $D_i/D_o=0.5$ . The eccentricity varies from 0.7 up to 0.9 in intervals of 0.05. For coupled problem simulations, accounting for heat transfer associated to turbulence, both Reynolds number and Prandtl number were kept constant,  $Re = 15000$  and  $Pr = 0.7$ . The boundary condition of the heat transfer problem was prescribed heat flux at the inner wall surface,  $q'' = 2000$  W/m<sup>2</sup> while the outer wall was kept insulated.

Numerical simulation has been performed using the URANS/LES approach in order to predict the main features of the turbulent flow. The working fluid was air and the Reynolds number was based on the hydraulic diameter  $D_h$ , the mean average velocity  $u_b$  and the kinematic viscosity of the fluid,  $\nu$ . Throughout the computations the density was kept constant. The specific model used was the DES-SST model, such model solves the flow field switching to LES turbulence model wherever possible, otherwise the k- $\omega$  SST model is then activated. The geometry of the problem presented in this work matches the one used by Choueiri and Tavoularis[1] in their experimental work. In our first simulation only the velocity field, the Reynolds stresses and the dynamic of the flow were computed and compared with the experimental work from the

mentioned authors. Afterwards, the Reynolds number was increased twice and the heat transfer problem was set up.

To assure the correct methodology was employed during the computations, a concentric case was also simulated, under the same Reynolds and Prandtl numbers. The results were then compared with the analytical equations presented by Gnielinski (2011).

The analysis of the results showed that the model used for the numerical simulations was successful in predicting the characteristics of the flow. The patterns of the velocity fluctuations and their quasi-periodic motions were correctly predicted by the code and presented good agreement with experimental data from the fluid dynamics studies of Choueri and Tavoularis[1].

The methodology used for the heat transfer case was validated through the analytical equations for the concentric case. After the validation of the methodology for the concentric case, the eccentric cases were simulated with the same boundary conditions ( $Re=15000$ ,  $Pr=0.7$ ,  $D_i/D_o = 0.5$  and constant heat flux  $q'' = 2000 \text{ W/m}^2$  and density, while the outer wall kept insulated). It was possible to find a direct correlation between the Nusselt number and the dynamic behavior of the flow. According to the results at the onset of the velocity fluctuations, the reduction of the area at the narrow gap no longer affects the heat transfer process strongly. For an optimal eccentricity, found in our case to be 0.85, it may be possible to maintain almost the same values of the Nusselt number that are found in the concentric case. The worst outcomes were found in the cases with eccentricities of 0,7 and 0,75 where the velocity fluctuations did not appeared just at the end of the channel. In these cases, the Nusselt number in the Narrow gap was decreased by around 75% in comparison with the concentric case.

## RESUMO

A transferência de calor convectiva e as características do escoamento em canais anulares é um fenômeno importante no campo da engenharia. Muitas das aplicações da engenharia te, canais concêntricos e excêntricos, como trocadores de calor, reatores nucleares, sistemas de energia solar, esfriamento de dispositivos eletrônicos. Alguns canais anulares aparecem como resultado de erros na fabricação ou na construção levando a ter desalinhamento das tubulações e assim o aparecimento dessas configurações geométricas com fendas estreitas. Nos dois casos é importante entender o comportamento do escoamento.

O intuito do trabalho é investigar o efeito das flutuações da velocidade nos coeficientes de transferência de calor para canais excêntricos usando simulação numérica. Os principais parâmetros geométricos do canal são o comprimento,  $L=1500$  mm e a razão dos diâmetros  $D_i/D_o=0.5$ . A excentricidade muda entre 0.7 e 0.9 em intervalos de 0.05. Para os problemas acoplados o número de Reynolds e o número de Prandtl foram mantidos constantes  $Re = 15000$  e  $Pr = 0.7$ . A condição de contorno para o problema de transferência de calor foi um fluxo de calor prescrito na parede interna  $q'' = 2000$  W/m<sup>2</sup> e a parede externa é mantida isolada.

Foram feitas simulações numéricas usando formulações URANS/LES com o intuito de ter uma previsão das principais características do escoamento turbulento. O fluido de trabalho foi ar e o número de Reynolds foi baseado no diâmetro hidráulico a velocidade média  $u_b$  e a viscosidade cinemática do fluido  $\nu$ . O modelo específico usado foi o modelo DES-SST, esse modelo resolve o campo de fluxo fazendo uma troca entre o modelo LES e o modelo  $k-\omega$  SST. A geometria do problema é a mesma usada pelo Choueiri e o Tavoularis [1] no seu trabalho experimental. Na nossa primeira simulação só o campo de velocidade, as Tensões de Reynolds e a dinâmica do escoamento foi simulada e comparada com o trabalho experimental. Depois o número de Reynolds foi incrementado e o problema de transferência de calor foi adicionado.

Para ter certeza que a metodologia usada era certa, foi simulado um caso concêntrico com o problema de transferência de calor. Os resultados

foram comparados com as equações analíticas apresentadas pelo Gnielinski (2011).

A análise de resultados mostrou que o modelo usado para as simulações numéricas teve sucesso ao prever as características do escoamento. O comportamento quase-periódico foi modelado corretamente pelo código e apresentou uma boa concordância com os resultados experimentais do Choueiri e o Tavoularis [1].

A metodologia usada para os casos com transferência de calor foi validada com as equações analíticas para o caso concêntrico. Após a validação da metodologia, os casos excêntricos foram simulados com as mesmas condições de contorno. Foi possível achar uma correlação direta entre o número de Nusselt e o comportamento dinâmico do escoamento. Segundo os resultados, após o início das flutuações de velocidade a redução da área não afeta fortemente o processo de transferência de calor. Foi achada uma excentricidade ótima  $e=0.85$  onde foi possível manter quase os mesmos valores do número de Nusselt que foram obtidos no caso concêntrico. Os piores resultados foram obtidos nas excentricidades de 0.7 e 0.75 onde as flutuações de velocidade não apareceram ou apareceram só no final do canal e o número de Nusselt apresentou reduções de até 75% comparado com o caso concêntrico.

## TABLE OF CONTENTS

1	INTRODUCTION.....	15
1.1	Motivation.....	15
1.2	Objectives .....	17
1.2.1	General Objective .....	17
1.2.2	Specific purpose .....	17
1.3	Chapters Organization .....	18
2	BIBLIOGRAPHIC REVIEW .....	19
3	FUNDAMENTAL EQUATIONS .....	30
3.1	Governing equations .....	30
3.1.1	Mass conservation.....	30
3.1.2	Momentum conservation .....	30
3.1.3	Energy equation.....	30
3.2	Turbulence models.....	33
3.2.1	k-w SST model .....	33
3.2.2	LES model .....	34
3.2.3	DES-SST model .....	34
3.3	Forced convection heat transfer.....	37
3.3.1	Nusselt number.....	37
3.3.2	Heat transfer in concentric channels.....	37
3.3.3	Heat transfer in eccentric channels.....	39
4	METHODOLOGY .....	40
4.1	Computational domain and mesh.....	40
4.2	Boundary conditions.....	42
4.2.1	Isothermal case .....	42
4.2.2	Heat transfer case .....	43
4.3	Turbulence Settings – DES-SST .....	44
4.4	Simulations performed .....	44
5	RESULTS AND DISCUSSION.....	46
5.1	Isothermal eccentric channel.....	46
5.1.1	Mean flow development.....	46
5.1.2	The dynamics of the flow – the strouhal for isothermal flow .....	49

5.2	Non-isothermal cases.....	51
5.2.1	Main velocity components in the narrow gap.....	51
5.2.2	Velocity contours and profiles.....	53
5.2.3	Fluctuation intensities.....	59
5.2.4	The dynamics of the flow – the strouhal number for non-isothermal flow	64
5.2.5	The coherent structures visualization - q-criterion.....	66
5.3	Heat transfer – THE NUSSELT NUMBER AND THE ECCENTRICITY	69
5.3.1	The Reference case.....	69
5.3.2	Eccentric channels.....	70
6	CONCLUSIONS.....	75
6.1	Future works.....	77
7	REFERENCES.....	79

## LIST OF FIGURES

Figure 2.1 Inner and outer friction factors of an eccentric channel with radius ratio of 5/6. [16] .....	20
Figure 2.2 Streak oscillations in the narrow gap for a constant Reynolds number and different eccentricities. [17].....	20
Figure 2.3 Velocity vector in the narrow gap. (a) Streamline projection. (b) $Re \approx 7800$ . [1].....	23
Figure 2.4 Flow rate at critical condition vs the radius ratio. Outer radius constant. [25].....	23
Figure 2.5 Turbulent friction factor for rectangular and triangular subchannels. [27] .....	24
Figure 2.6 Variation of the average Nusselt number for a case with heat transfer in the inner wall and the outer wall insulated. Prandtl number, 0.73. [4].....	26
Figure 2.7 Fully developed temperature distributions for a concentric case with a constant Reynolds number and a varying Prandtl number. [32].....	27
Figure 2.8 Influence of radius ratio in the entrance length. [33].....	28
Figure 4.1 Computational domain. (a) Schematic view of the channel. (b) Mesh of the cross section. (c) Cross-section of the channel. ....	41
Figure 4.2 Boundary conditions of the isothermal case .....	42
Figure 4.3 Boundary conditions of the non-isothermal case.....	43
Figure 5.1 Velocity fluctuations of the main components, the blue line represents the fluctuations along the channel and the red line the mean of the fluctuations. (a) Stream-wise direction. (b) $v$ direction. (c) Span-wise direction. ....	48
Figure 5.2 Velocity fluctuations of the three main components at five measurement points obtained experimentally by Choueiri and Tavoularis [1]. (a) Stream-wise fluctuations. (b) Span-wise fluctuation at the measurement points. (c) Velocity fluctuations in the $w$ direction.....	49
Figure 5.3 Stream-wise and span-wise velocity fluctuations at five seconds of simulation. (a) $x/Dh=38$ , end of the FG region. (b) $x/Dh=42$ , beginning of the RM region. (c) $x/Dh=53$ , end of the RM region. ....	50
Figure 5.4 Variation of the Strouhal number along the channel .....	51
Figure 5.5 Comparison of the streamwise velocity $u_m/u_b$ along the channel	52
Figure 5.6 Comparison of the spanwise velocity $w_m/u_b$ along the channel...	53
Figure 5.7 Velocity contours in the streamwise direction in the transversal plane located at $x/Dh=50$ . (a) Reference case. (b) Case A. (c) Case B. (d) Case C. (e) Case D. (f) Case E.....	55
Figure 5.8 Velocity profiles in the narrow gap at different instances along the channel. (a) Reference case. (b) Case A. (c) Case B. (d) Case C. (e) Case D. (f) Case E. ....	58
Figure 5.9 Streamwise velocity contours for the D case. (a) $x/Dh=20$ . (b) $x/Dh=40$ . (c) $x/Dh=50$ .....	59

Figure 5.10 Streamwise velocity intensity contours at $x/D_h=50$ . (a) Reference Case. (b) Case A. (c) Case B. (d) Case C. (e) Case D. (f) Case E. ....	61
Figure 5.11 Spanwise velocity intensity contours at $x/D_h=50$ . (a) Reference Case. (b) Case A. (c) Case B. (d) Case C. (e) Case D. (f) Case E. ....	63
Figure 5.12 Strouhal number in the streamwise and spanwise directions at $x/D_h=30$ and $x/D_h=50$ .....	66
Figure 5.13 Fast Fourier Transform graphs (a) Eccentricity 0.8 (b) Eccentricity 0.85 (c) Eccentricity 0.9.....	65
Figure 5.14 Visualization of the Q- criterion. (a) Reference case. (b) Case A. (c) Case B. (d) Case C. (e) Case D. (f) Case E.....	68
Figure 5.15 Axial temperature variations of the concentric case .....	69
Figure 5.16 Comparisson of surface temperature along the channel .....	71
Figure 5.17 Comparisson of the variation of the Nusselt number in the azimuthal direction.....	73
Figure 5.18 Variation of the Nusselt number in the azimuthal direction for the cases D and E at two different positions along the channel $x/D_h=10$ and $x/D_h=50$ .....	74

## LIST OF TABLES

Table 4.1 Distance of the first element near the wall in all the cases .....	41
Table 4.2 Coordinates of the measurement points for the experimental case [1] .....	42
Table 5.1 Denomination of the different eccentricity cases. ....	46
Table 5.2 Numerical and analytical results of the Nusselt number .....	70

# 1 INTRODUCTION

## 1.1 Motivation

Turbulent flow is one of the problems in the fluids mechanics field that has been widely studied over the years. As a result of its vast application in the engineering field that responds to this type of behavior, will be certainly studied for many other years. In the engineering field is quite easy to find applications of turbulent flow in non-circular channels. A wide variety of mechanical systems used in industrial applications are constituted by a simple stationary annulus pipe whose fluid passes through the narrow gap between inner and outer cylindrical walls. Counter, concurrent flow, shell and tube heat exchangers, electrical motors, generators, cores of nuclear reactors and more are some examples of devices that use annular passages and narrow gaps . In many cases, the design tolerances and manufacturing limits may cause a misalignment, creating some eccentricity between inner and outer rods. This is the reason why the eccentric annulus and the non-circular passages have become of interest to researchers. On the other hand, the design project itself leads to the genetry that contains tight passages, that might be characterized as a narrow gap.

A narrow region connected to one or more wide regions is described as a compound channel. In the narrow regions the viscous effects are predominant giving rise to a new mass distribution inside the channel that is different in comparison to that one found in single channels. Furthermore, the turbulence characteristics itself is also affected by the channel configuration. At the gap vicinity the Reynolds Stresses and the mixing process are enhanced as consequence of the large scale motions that dominate the region [2].

Industrial equipment with narrow passages that can be classified as a kind of compound channel needs a great understanding of the dynamics of the flow and the friction factor, velocity profile and shear stresses fields. In some industrial applications is also important to know the behavior of the heat transfer coefficients, and how such coefficients are affected by the turbulence and the geometric parameter of the equipment. Furthermore, the design of the project must take into account the peculiarities of the turbulence effects on the heat transfer problem, otherwise, the operational reliability of the equipment may be seriously affected.

The laminar and turbulent flow in circular pipes has been vastly studied over the years and it was possible to develop equations that describe the dynamic characteristics of the flow accurately. In the same way, concentric channels are examples of geometry configurations whose analytical solutions are successfully applied to describe the flow field and the thermal behavior facing some particular boundary condition. The main reason lies on the symmetry of the geometries, and therefore, the symmetry of the flow. In the eccentric annulus pipe case, this symmetry no longer exists and the cross-sectional area reminds the idea of the compound channel concept. The mean average velocity is higher away from the narrow gap. Due to the asymmetry of the geometry, the equations that describe the dynamic behavior in circular and concentric pipes are not able to predict the flow features in the eccentric case [3].

Despite of the asymmetry of the flow, a wide variety of studies have been made in order to know how the asymmetry of the transversal section and the geometry characteristics can influence in the friction factor, maximum velocity, shear stress fields, mean average velocity, friction velocity and mass distribution. One of the characteristic, very well reported in previous works, is the friction factor decreasing as the eccentricity increases. Moreover, studies have shown that flow asymmetry increases as the eccentricity increase, regardless the Reynolds number [4][5][6][7][8]. This kind of behavior appears to be independent of the geometry of the cross-section shape, since it has been encountered in triangular and rectangular ducts as well [9].

The analytical solutions for concentric cases under laminar flow have been better developed and studied non-circular passages or eccentric annuli with heat transfer. Reynolds and co-workers [10] presented the solution for the heat transfer problem in fully developed laminar flow in concentric annulus. In the same field, Gnielinski [11] presented analytical equations to obtain the friction factor and Nusselt number for fully developed turbulent flow in concentric annuli taking into account the geometry of the problem ( $D_i/D_o$  ratio), the Reynolds number, the Prandtl number and the thermal boundary conditions type prescribed. Such work provides a set of specific constants to be used depending on the thermal boundary conditions of the problem (constant heat flux, constant surface temperature, etc). For the case of eccentric channels and

others non-circular passages, there are some studies developed, however, a lack of information and research still remains. Studies performed in eccentric case, with different Reynolds numbers,  $D_i/D_o$  ratio and thermal boundary conditions, have shown that the effect of increasing eccentricity generally leads to a decrease of Nusselt number compared with the concentric case under the same geometrical, thermal, and fluid dynamics boundary conditions [4][12][13][14].

This work aims to perform a numeric simulation of a turbulent flow in eccentric annulus passages using a commercial finite volumes platform. The main geometric parameters of the channel are the length,  $L=1500$  mm, the diameter ratio  $D_i/D_o=0.5$  and the eccentricity [0.7, 0.75, 0.8, 0.85, 0.9]. The computations were performed under a Reynolds number of 15000. To perform the coupled problem, heat flux  $q''=2000$  W/m<sup>2</sup> was imposed at the inner wall and the outer wall insulated. The Prandtl number was set to 0.7 and the density of the fluid was kept constant for all simulations. Both Reynolds and Prandtl numbers were kept constant throughout the computations, regardless the geometry. The same boundary condition of constant heat flux in the inner wall and the outer wall insulated is applied in a concentric channel. A comparison between the numerical results and the analytical equations, available in the literature, for the concentric case was carried out in order to validate the methodology proposed.

## **1.2 Objectives**

### **1.2.1 General Objective**

The present work has the main goal to investigate the process of developing turbulent flow in eccentric channels under heat transfer processes. To achieve such goals, prescribed heat flux was imposed at inner wall and the outer wall insulated.

### **1.2.2 Specific purpose**

The specific goals of this work are:

- Perform a numeric simulation of the problem studied experimentally by Choueiri and Tavoularis [1] and compare the results. In this section incompressible, turbulent and isothermal flow will be simulated.

- Increase the Reynolds number, adding the heat transfer process and perform a turbulent flow simulation for concentric pipe flow. The numerical predictions will be compared with analytical solutions available in literature.
- Validate the methodology used for the heat transfer problem with analytical equations for previous works.
- Simulate non-isothermal flow in eccentric channels with  $D_i/D_o$  ratio of 0.5. and eccentricities varying from 0.7 to 0.9, to assess how the turbulence and the velocity patterns at the gap vicinity affect the local Nusselt number.

### **1.3 Chapters Organization**

This work is presented in seven chapters. Followed by the introduction, chapter two presents the previous works in concentric and eccentric channels taking into account just purely flow dynamics and heat transfer problems through a bibliographic review.

Chapter three presents the fundamental theory of turbulence as well as the explanation of the turbulence models applied in the numerical simulations.

Chapter four explains the methodology used in order to perform the simulations as well as the geometry used and the boundary conditions applied to the problem.

The results, analysis and discussion are presented in the chapter five. Chapters six and seven, presents the conclusions and references respectively.

## 2 BIBLIOGRAPHIC REVIEW

The interest in the understanding of the flow in annular passages arises because of the vast applications in engineering and even in nature that have this kind of geometries. Every day the technology creates new applications for these channels, such as cooling of electronic devices and industrial machinery. As regards the healthy sciency catheterized arteries in the medicine field are thought as a concentric pipe flow.

Several studies on annular passages have been made along the last fifty years. One of the first reference studies of these geometries was the work developed by Redberg and Charles [15]. They made a numerical study of laminar flow in a circular pipe with eccentricities from 0 up to 1 and  $D_i/D_o$  ratio varying between 0.1 and 0.9. Their outcomes were compared with analytical solutions available at that time. The main conclusions of the work was that for lower  $D_i/D_o$  ratio, the sensitivity to the eccentricity increases making higher the changes in the volumetric flow rate at a given pressure gradient [15].

Soon after, Snyder and Goldstein [16] presented an exact solution of the velocity distribution for a fully developed turbulent flow in an eccentric channel. From this solution was also possible obtain expression for local shear stress distribution and friction factors in each wall and the overall friction factor. Besides, they concluded that the wall stress is higher in the regions of small gaps, the local friction factor is lower in the outer wall compared with the inner wall in the same angle position, as shown in Figure 2.1 [16].

Piot and Tavoularis made another study in laminar regime. They studied the flow instabilities that appeared in the narrow gap of the eccentric channel with  $D_i/D_o$  ratio of 0.282 and Reynolds numbers higher than 1200. They noticed that the streak oscillations in the narrow gap become stronger as the eccentricity increased as shown in Figure 2.2[17]. They compared the critical Reynolds number in both the narrow and the wider gap and concluded that in the narrow gap, the critical Reynolds number increases with the eccentricity. In the case of the wider gap, seems to be insensitive to low variations of the eccentricity.

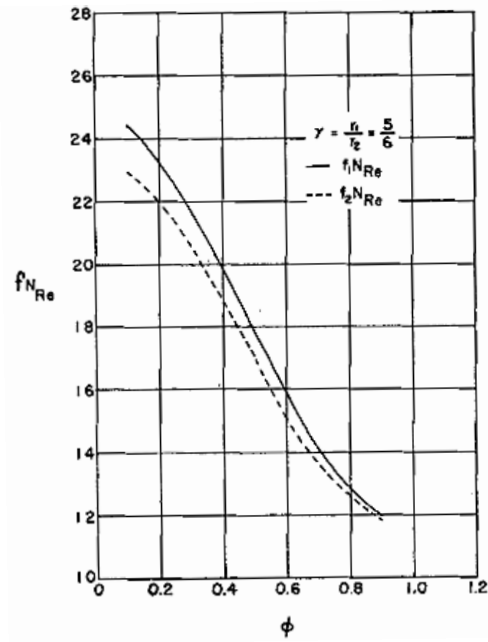


Figure 2.1 Inner and outer friction factors of an eccentric channel with radius ratio of 5/6.[16]

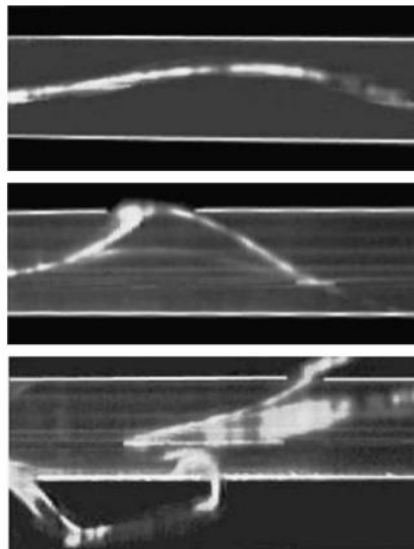


Figure 2.2 Streak oscillations in the narrow gap for a constant Reynolds number and different eccentricities.[17]

An impressive amount of studies have also been devoted to the turbulent regime in concentric and eccentric annulus, in order to understand how the radius ratio and the eccentricity can affect the development and behavior of the flow. Douglas[3] made an experimental work using Reynolds number ranging from 20000 to 55000 and eccentricities varying from 0 up to 0.5. He found out

that the friction factor decreases with increasing of the eccentricity. This is one of the principal characteristics found in eccentric channels and the same behavior has been encountered by others authors over the years [5][7].

Another important experimental work was developed by Quarmby [18] in a concentric channel using different radius ratio and a Reynolds number, ranging from 6000 up to 90000. He found that the friction factor is independent of the radius ratio. However, the location of the point of maximum velocity was found to depend on both Reynolds number and radius ratio. Performing experiments in a concentric channel, Clump and Kwasnoski [19] implemented a diffusivity model to predict the turbulence in these geometry. They compared the velocity distributions obtained by their model with previous works from other authors and found a great agreement with the results predicted. Lawn and Elliot [20] studied experimentally a concentric channel using as radius ratio 0.088, 0.176 and 0.396. They found that the radius where is found the zero shear stress is independent of the Reynolds number and also noticed that the friction factor in the concentric case is between 5% and 8.5% above than that one found in a pipe flow. Two years after, Rehme [21] made an experimental work, which presented disagreement with the result found by Quarmby [18]. In his paper Rehme [21] concluded that the pressure drop coefficients increase slightly with increasing radius ratio and the friction factor decreases with increasing radius ratio.

In turbulence modeling, the isotropic two equation models have become industry standard models and are commonly used for most types of engineering problems. Two equation models include two extra transport equations to represent the transport of turbulent properties of the flow. This allows to know the history effects like convection and diffusion of turbulent energy. The ability of the two equation models to predict important turbulent parameters such the turbulent kinetic energy, eddy viscosity and dissipation has also been studied and compared with experimental data. A comparison between  $k - \omega$  model and the  $k - \varepsilon$  model was performed by Speziale and co-workers [22]. They found that the  $k - \omega$  model neglects an exact viscous cross-diffusion term and does not damp the destruction of the dissipation term near the wall. Due to these simplifications the turbulent kinetic energy prediction near the boundary are not very successful although it gives adequate predictions for the skin friction and

turbulence statistics away from the wall. Besides, they proposed a  $k - \tau$  model including the viscous term and introducing near wall damping functions. Azouz and co-workers[23] compared both  $k - \tau$  model and the mixing-length model for concentric and eccentric annuli. The  $k - \tau$  model performs equally well for concentric annuli, but in the case of eccentric channels, the  $k - \tau$  seemed to perform better than the mixing-length model.

Some years ago, Chung [24] made a numerical simulation of a concentric channel with a Reynolds number of 8900 emphasizing his investigation in the transverse curvature effect on near-wall turbulent structures. He found that the turbulent structures near the outer wall are more activated than those near the inner wall and the inner wall supplies relatively less turbulent kinetic energy than the outer wall. This fact can be attributed to the different vortex generation process that occurs in each wall.

Most papers have been focused the attention on the fully developed regime condition, but in many engineering applications is also important to take into account the entrance region flow. In the entrance region the flow has not yet hydrodynamically fully developed. In this context, Choueiri and Tavoularis [1] made a very thorough experimental study in an eccentric channel with a  $D_i/D_o$  ratio of 0.5, and eccentricity of 0.8 and a Reynolds number of 7300 using an aqueous solution of ammonium thiocyanate ( $\text{NH}_4\text{SCN}$ ) as a work fluid. They named three main regions from the beginning of the channel to the end. These three regions presented specific characteristics of the flow velocity fluctuations patterns, which change as the stations get farther from the channel's entrance. The Figure 2.3 shows the flow development along the channel at the narrow gap of the eccentric annuli. Parameters as the mean velocity fluctuations, Strouhal number and convection velocity of the flow along the channel length were also studied.

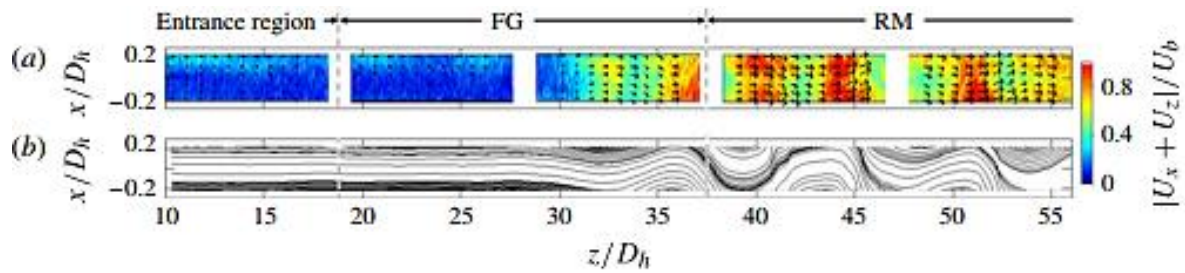


Figure 2.3 Velocity vector in the narrow gap. (a) Streamline projection. (b)  $Re \approx 7800$ . [1]

Using energy gradient method, developed in previous works, Dou and co-workers[25] calculated the critical condition for turbulent transition in a concentric annulus using various radius ratio. They observed that the critical flow rate, as well as, the critical Reynolds number for the onset of turbulent transition increases with increasing of the radius ratio. Figure 2.4 shows the results found by the authors in order to validate the influence of the radius ratio( $k$ ) in the critical condition for turbulent transition  $Q_c$ . The inner rod creates instability for radius ratio ranging from 0.12 up to 0.18, enhancing the stability for radius ratio higher than the same values.

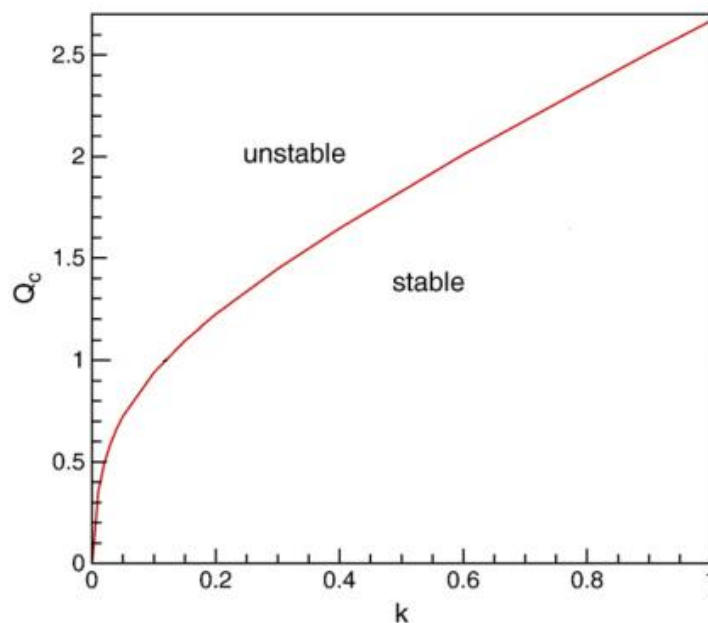


Figure 2.4 Flow rate at critical condition vs the radius ratio. Outer radius constant. [25]

As the annular channels can be considered as non-circular passages, other geometries with narrow gap regions are also focus of interest, since channels with tight gaps, but different geometries, are widely used in engineering applications. An experimental study on the gap region created by

four half rods located in a cross configuration is presented by Cajarilescov and Todreas[26]. They implemented an algebraic stress turbulence model for a Reynolds number of 27000, in order to take into account the secondary flow effects. Measurements with a Laser Doppler Anemometry (LDA) for the axial velocity distributions and turbulence kinetic energy were also performed. It was found that the model used can provide reasonable predictions of axial velocity, friction factor and wall shear stress distributions. The results of the experiments were compared with the analytical results as well as other experimental data from previous authors.

Bae and Park[27] developed an analytical calculation to predict the turbulent friction factor in a rod bundle, deriving the geometric parameters integrating the law of the wall over each subchannel. They found that the friction factor converges to a constant value, regardless the geometry of the channel. At the central subchannel the friction factor was found to increase constantly as the rod distance ratio increases, as shown in Figure 2.5.

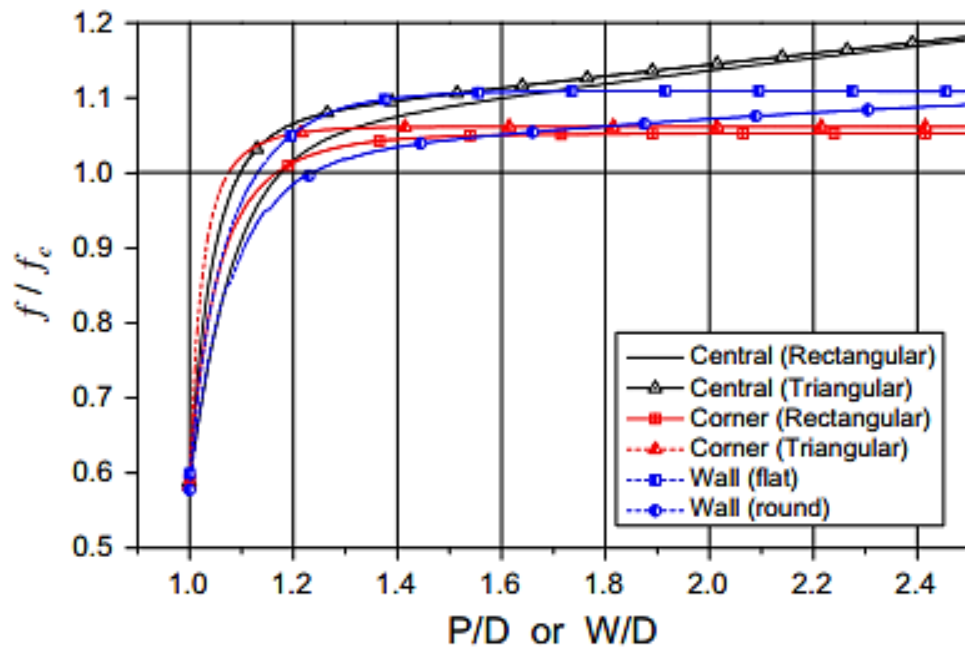


Figure 2.5 Turbulent friction factor for rectangular and triangular subchannels.

[27]

Bertocchi and co-workers[28] made an experimental work based on Laser Doppler Anemometry (LDA) to measure the turbulent quantities and the friction factor at gap region between two rods, under a Reynolds number ranging from 600 up to 30000. They noticed that as the flow rate decreases, a peak in the root mean square of the streamwise velocity is found at the center

of the gap as a consequence of the coherent structures crossing the gap, implying in the cross flow enhancement. They also observed that as the Reynolds number is decreased the structures are found to appear further away from the entrance of the main sub channel. Besides, it was found that one of the mechanism that may increase the heat transfer coefficients are the large coherent structures that can occur across the gap between two rods.

Similar to the cross-flow found in the gap by Bertocchi [28], a study of a pressurized water reactor (PWR) sub-channel was made by Lakehal [29] using a LES model. It was found a low influence of the Reynolds number in the narrow gap and a strong secondary flow motion, this secondary flow seemed to have more importance than the principal flow and exceeded the turbulence counterpart near the wall.

The principal applications of the eccentric annuli, geometries, are found in equipment that works with heat transfer. The heat exchangers, nuclear reactors, thermal storage systems, boilers, solar energy systems are just some examples of the wide variety of applications that are constituted by this kind of geometries. The interest in the understanding the heat transfer process in non-circular channels arises from the need of controlling, increasing and improving the heat transfer process. When the non-circular passage is a consequence of manufacture errors, the better understanding of the process can lead to better practices in damage control. In the case of enhancement of the heat transfer, it is also important to know how the flow dynamics and geometric parameters affect the heat transfer coefficients.

Purely flow dynamics in non-circular passages along with the heat transfer process have been studied over the years. Deissler and Taylor [4] presented an analytic method for concentric and eccentric annuli passages flow, analyzing the dynamics of the flow and the heat transfer problem. For the dynamics of the flow, it was found that the line of maximum velocity lies closer to the inner wall than to the outer wall. The friction factor was found to decrease as the eccentricity increase [3][5][7]. For the case of maximum eccentricity the friction factor was found to be up to 70% of the value obtained for the concentric case. In the case of the heat transfer problem, prescribing insulated outer wall, the average Nusselt number in the concentric case has a value slightly higher compared with the circular tube. However, as the eccentricity increases the

Nusselt number decreases, as shown in Figure 2.6. Despite that the local Nusselt number was not obtained in the different gap regions, the behavior presented in the figure below may be attributed to the different velocities distributions that appear when the eccentricity increases.

Non-isothermal flow was also target of investigation in the papers published by Dreissler and Taylor [4] and Lee and Barrow [30]. Both works studied the heat transfer in annuli passages, being the inner wall heated and the outer one kept insulated. Studies were carried out by using different radius ratio and Reynolds numbers. They concluded that the influence of the eccentricity on the Nusselt number is similar to the friction factor. The Nusselt number decreases when the eccentricity increases, being such behavior even more evident in the annulus pipe flow for lower radius ratio.

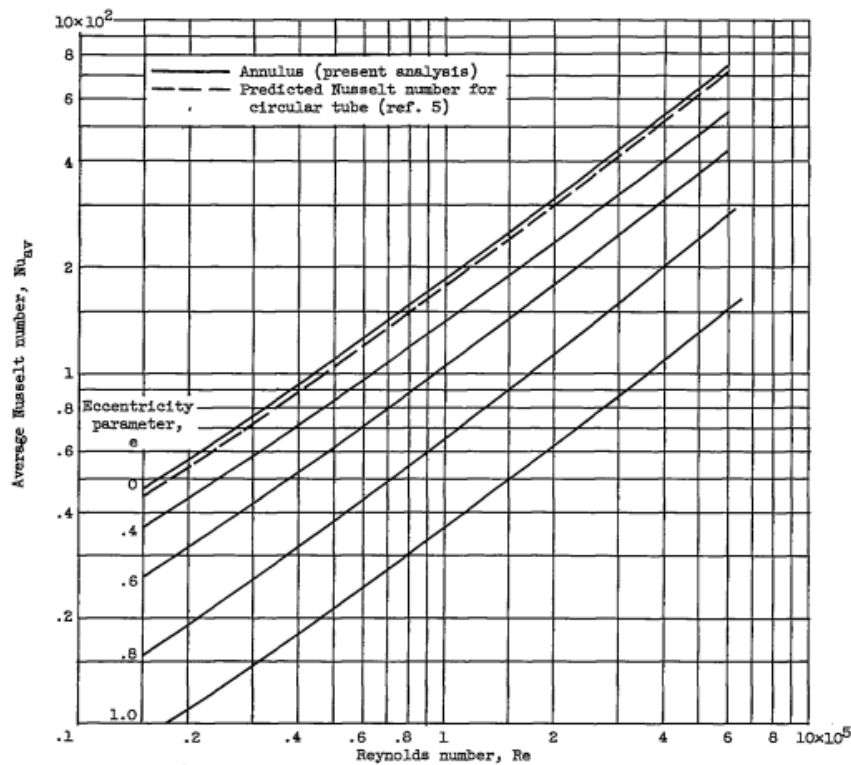


Figure 2.6 Variation of the average Nusselt number for a case with heat transfer in the inner wall and the outer wall insulated. Prandtl number, 0.73[4].

In 1968, Cheng and Hwang [31] studied the heat transfer problem for eccentric channels under laminar flow using as boundary condition uniform heat flux in both inner and outer walls. The purpose of the work was to present a solution without using bipolar transformation and they decided to apply a

Simpson's rule for integration having excellent agreement with the results obtained for previous works [31]. The same year, Wilson and Medwell employed the analogy of heat and momentum transfer in a concentric case under turbulent flow, analyzing different radius ratio and different Prandtl numbers. The results of the work showed that the friction factor depends only on the Reynolds number for radius ratios higher than 0.2. The Figure 2.7 presents the variation of the temperature distributions found by the authors, they concluded that at low Prandtl numbers the more rounded profiles are obtained as consequence of the dominance of molecular diffusion. Increasing the Reynolds number decreases the thickness of the sublayer which leads to the square shape of the profiles [32].

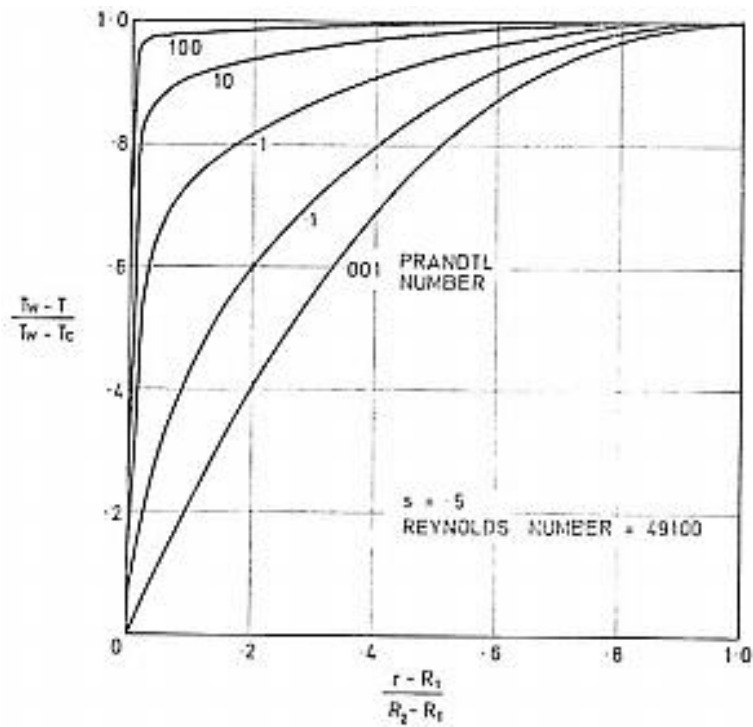


Figure 2.7 Fully developed temperature distributions for a concentric case with a constant Reynolds number and a varying Prandtl number. [32]

As mentioned before, many applications of non-circular passages such as heating and cooling applications starts at the duct entrance or before the fully development conditions. Many studies are found considering a fully developed regime. However, few works have taken into account the entrance region. In this scenario, Quarmby and Anad [33] suggested a solution for either the thermal fully developed entrance region for a concentric annuli with different

radius ratio, Prandtl numbers and uniform heat flux on either surface. The entrance length showed to be considerably shortened for Prandtl numbers superior to one. In the Figure 2.8, they stressed the relationship between increasing the radius ratio  $b$  and the entrance length  $x^+$  for both cases of heated inner or outer surface. It is noticeable that with the increasing of  $b$ , the entrance length decreases but it is also important to see that this effect is more noticeable for the heated inner wall compared to the heated outer wall.

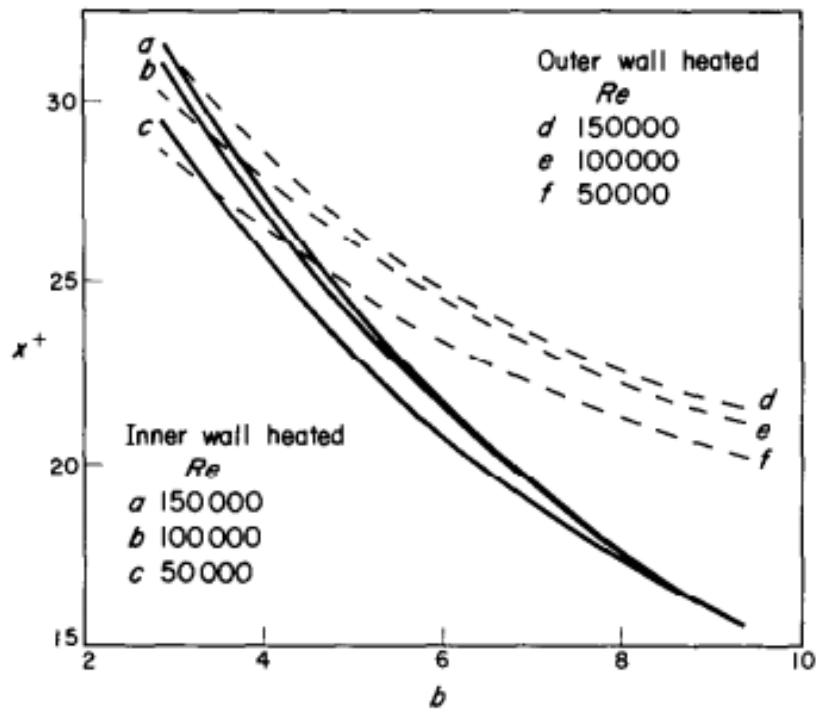


Figure 2.8 Influence of radius ratio in the entrance length. [33]

Nikitin and co-workers [8] used Direct Numerical Simulations (DNS) to carry out computations of the flow in eccentric tube ( $e=0.50$ ; eq. 2.1) under turbulent flow at  $Re=8000$ . The authors observed that in the narrowest gap the flow may be considered as laminar in terms of the local Nusselt number but this consideration is no longer possible in terms of the intensity of temperature fluctuations. This oscillations appeared to be significantly higher near the inner wall compared to the outer wall

$$e = \frac{2\Delta y}{D_o - D_i} \quad (2.1)$$

Where:

$\Delta y$  = Distance between centers

$D_o$  = Outer diameter

$D_i$  = Inner diameter

In more recent years, Volker Gnielinski [11] presented an analytical equation for the calculation of the friction factor and the Nusselt number IN concentric cases taking into account a diameter ratio( $D_i/D_o$ ), the Reynolds number, the Prandtl number and the thermal boundary conditions of the heat transfer problem. Some years later, Dawood and co-workers [34] made a bibliographic review of different experimental and numerical works studying the enhancement of thermal performance. In this review they presented natural convective and forced convective heat transfer cases for both concentric and eccentric annuli with horizontal, vertical and inclined configurations. From the results presented in this review was possible to validate the Nusselt number decreasing as a function of the eccentricity increasing, whenever forced convection was imposed for horizontal channel. On the other hand, in vertical channels some results showed that the local and averaged Nusselt number increases as direct function of the eccentricity.

Chung and Jin Sung [35] solved non-isothermal flow in the same geometry presented in their work of 2002 in order to investigate the effect of the curvature of the channel on the turbulence and thermal parameters near the wall. They found that overall turbulent thermal statistics were larger in the outer wall compared to the inner wall associating such results to the transverse curvature of the wall. It was also noticed by the authors that this tendency was more evident for small  $D_i/D_o$  ratios.

Jian Su and co-workers [36] developed an analytical method based on the law of the wall for velocity and temperature for the prediction of friction factor and Nusselt number in rod bundles arranged in square and hexagonal arrays. They compared their results with those ones available in literature, achieving great agreement. In the square array, the proposed model slightly under predicted the Nusselt number but still holding a good agreement. The results obtained for the hexagonal array was found to match with previous works found in the literature.

### 3 FUNDAMENTAL EQUATIONS

#### 3.1 Governing equations

In this chapter it will be briefly presented the main equations which rule the mass, energy and momentum conservation in a fluid flow.

##### 3.1.1 Mass conservation

For compressible and non-stationary flow, the continuity equation also known as mass conservation equation is written as:

$$\frac{\partial \rho}{\partial t} + \frac{\partial}{\partial x_i} (\rho u_i) = 0 \quad (3.1)$$

where:

$\rho$  = density of the fluid.

$u_i$  = velocity component in the orthogonal directions.

$x_i$  = spatial coordinates.

$t$  = time.

##### 3.1.2 Momentum conservation

The equation of the momentum conservation is obtained from the Newton's second law of motion, which says that the variation of the momentum is equal to the summation of the external forces acting on a fluid mass. In the equation (3.2) the letter F represents additional external forces also acting in the fluid. The terms at the right of the equation are the pressure  $P$ , the normal stresses and the shear stresses applied to the surfaces of the control volume.

$$\rho \frac{\partial u_i}{\partial t} + \rho u_j \frac{\partial u_i}{\partial x_j} = -\frac{\partial P}{\partial x_i} + \frac{\partial}{\partial x_i} \left[ 2\mu \frac{\partial u_i}{\partial x_i} - \frac{2\mu}{3} \left( \frac{\partial u_i}{\partial x_i} + \frac{\partial u_j}{\partial x_j} \right) \right] + \frac{\partial}{\partial x_j} \left[ \mu \left( \frac{\partial u_i}{\partial x_j} + \frac{\partial u_j}{\partial x_i} \right) \right] + F \quad (3.2)$$

##### 3.1.3 Energy equation

The continuity and momentum equations are in most cases enough to solve a pure dynamic problem. However, when the heat transfer problem is added, the temperature field solution requires additional equation.

The first law of thermodynamics also known as the energy equation is in charge of lead us to accomplish this objective. The first law of thermodynamics establishes that the rate of energy accumulation in the control volume is equal to five terms listed below:

1. The net transfer of energy by fluid flow.

2. The net heat transfer conduction.
3. The rate of internal heat generation.
4. The net work transfer from the control volume to its environment.

The energy equation can be expressed in terms of enthalpy, turbulent kinetic energy or temperature. In the equation (3.3) is presented the temperature formulation of the energy equation in terms of the specific heat ( $C_p$ ) and constant pressure ( $P$ ). For problems where the fluid is incompressible ( $\beta=0$ ), the conductivity ( $k$ ) is constant, does not exist internal heat generation ( $q'''=0$ ) and the viscous dissipation ( $\mu\Phi$ ) is negligible, the energy equation is written as in equation (3.4).

$$\rho C_p \frac{DT}{Dt} = \nabla \cdot (k\nabla T) - \beta T \frac{DP}{Dt} + \phi + q''' \quad (3.3)$$

$$\rho C_p \left( \frac{\partial T}{\partial t} + \nabla \cdot (T\vec{V}) \right) = \nabla(k\nabla T) \quad (3.4)$$

As it is known, the Navier-Stokes equations can be applied to laminar and turbulent flows, but in the case of turbulence, with all the details that occurs in small scales is no longer possible to make a direct discretization of the Navier-Stokes equations [39]. The solution presented by Reynolds [40] for the condition named for turbulence, is to decompose all quantities into two parts; a mean averaged quantity, represented as the quantity with an overbar and a fluctuating field, represented with and apostrophe as in equation (3.5)

$$\begin{aligned} P &= \bar{P} + P' \\ \rho &= \bar{\rho} + \rho' \\ T &= \bar{T} + T' \\ u_i &= \bar{u}_i + u'_i \end{aligned} \quad (3.5)$$

The overbar used in the previous equation to indicate a mean value, is also a symbol of a linear mathematical operator. The equations (3.6) to (3.9) presents the properties of this operator. [41]

$$\begin{aligned}\overline{a} &= \overline{\overline{a} + a'} = \overline{\overline{a}} + \overline{a'} = \overline{a} + \overline{a'} \\ \overline{a'} &= 0\end{aligned}\quad (3.6)$$

$$\overline{\overline{ab}} = \overline{\overline{ab}} = \overline{ab} \quad (3.7)$$

$$\overline{\overline{ab'}} = \overline{\overline{ab'}} = \overline{ab'} = 0 \quad (3.8)$$

$$\overline{ab} = \overline{(\overline{a} + a')(\overline{b} + b')} = \overline{\overline{ab}} + \overline{\overline{ab'}} + \overline{\overline{ba'}} + \overline{a'b'} \quad (3.9)$$

Employing the decomposition followed by the averaging process in the equation (3.1), we obtain:

$$\frac{\partial \overline{\rho}}{\partial t} + \frac{\partial}{\partial x_i}(\overline{\rho u_i}) = \frac{\partial(\overline{\rho} + \overline{\rho'})}{\partial t} + \frac{\partial}{\partial x_i}(\overline{(\overline{\rho} + \overline{\rho'})(\overline{u_i} + \overline{u_i'})}) \quad (3.10)$$

Applying the rules presented in equations (3.6) to (3.9) in the equation (3.10) leads to the expression presented in equation (3.11). Assuming an incompressible and stationary flow, it is obtained the expression (3.12).

$$\frac{\partial \overline{\rho}}{\partial t} + \frac{\partial}{\partial x_i}(\overline{\rho u_i}) = \frac{\partial \overline{\rho}}{\partial t} + \frac{\partial}{\partial x_i}(\overline{\rho u_i} + \overline{\rho' u_i'}) \quad (3.11)$$

$$\frac{\partial \overline{u_i}}{\partial x_i} = 0 \quad (3.12)$$

In the same way, the momentum and energy equations for incompressible flow can be re-written as:

$$\frac{\partial \overline{u}}{\partial t} + \frac{\partial(\overline{u_i u_j})}{\partial x_j} = -\frac{1}{\rho} \frac{\partial \overline{P}}{\partial x_i} + \nu \frac{\partial^2 \overline{u_i}}{\partial x_j^2} + \frac{\partial \tau_{ij}}{\partial x_j} \quad (3.13)$$

$$\frac{\partial \overline{T}}{\partial t} + \frac{\partial}{\partial x_i}(\overline{u_i T}) = \frac{\partial}{\partial x_i} \left( \alpha \frac{\partial \overline{T}}{\partial x_i} - (\overline{u_i' T'} + \overline{u_i T'} + \overline{u_j' T'} + \overline{u_j T'} - \overline{u_j T}) \right) \quad (3.14)$$

Where,

$\alpha$ =Thermal diffusivity"

$\tau_{ij}$ = Reynolds stress tensor

$\overline{u_i' T'}$ = Sub-grid turbulent Flux

$\overline{u_i T'} + \overline{u_j' T'}$ = Cross turbulent flux

$\overline{u_j T'} - \overline{u_j T}$ = Leonard's turbulent flux

In the equation (3.13) the first term in the right side of the equation corresponds to the momentum transference due to the pressure gradients. The second one is related to the momentum transference due to the velocity gradients and viscosity. And the third one is the Reynolds stress tensor that represents the momentum transference due to the velocity fluctuations.

## 3.2 Turbulence models

### 3.2.1 k- $\omega$ SST model

The Shear-Stress Transport ( $k-\omega$  SST) model was developed by Menter [42] to use the advantages of the classic  $k-\omega$  model in the near-wall regions and the advantages of the  $k-\varepsilon$  model in the regions far from the wall. In order to attach both turbulence models, the  $k-\varepsilon$  is converted into a  $k-\omega$  formulation. The  $k-\omega$  SST model has as characteristic a blending function which is 1 in the boundary layer region using the  $k-\omega$  model and zero in the regions outside of the boundary layer, activating the  $k-\varepsilon$  model.

Besides, the  $k-\omega$  SST model uses a damped cross-diffusion derivative term in the  $\omega$  equation and the turbulent viscosity is modified to take into account the transport of the turbulent shear stress [43].

The formulation of the  $k-\omega$  SST model are presented in the following equations, the transport equation for the kinetic energy  $k$  and the turbulent frequency  $\omega$ , respectively:

$$\frac{\partial(\rho k)}{\partial t} + \frac{\partial(\rho \bar{u}_i k)}{\partial x_i} = \frac{\partial}{\partial x_i} \left[ \left( \mu + \frac{\mu_t}{\sigma_{k2}} \right) \frac{\partial k}{\partial x_i} \right] + P_k - \beta' \rho k \omega + P_{kb} \quad (3.15)$$

$$\frac{\partial(\rho \omega)}{\partial t} + \frac{\partial(\rho \bar{u}_i \omega)}{\partial x_i} = \frac{\partial}{\partial x_i} \left[ \left( \mu + \frac{\mu_t}{\sigma_{\omega 2}} \right) \frac{\partial \omega}{\partial x_i} \right] + (1 - F_1) 2\rho \frac{1}{\sigma_{\omega 2} \omega} \frac{\partial k}{\partial x_i} + \alpha_2 \frac{\omega}{k} P_k - \beta_2 \rho \omega^2 + P_{\omega b} \quad (3.16)$$

Where:

$\beta', \beta_2, \alpha_2, \sigma_{k2}, \sigma_{\omega 2}$  are constants.

$P_{kb}, P_{\omega b}$  are source terms.

$P_k$  is the turbulence generation due to viscous forces.

The turbulent viscosity term in the  $k-\omega$  SST model is expressed by the following equation:

$$\mu_t = \frac{a_1 k}{\max(a_1 \omega, S F_2)} \quad (3.17)$$

In the equation (3.17) the term S is an invariant variable of the rate of deformation tensor and the term  $F_2$  is the second blending function and it is defined as follows:

$$F_2 = \tanh \left[ \max \left( \frac{2\sqrt{k}}{\beta^* \omega y}, \frac{500\nu}{y^2 \omega} \right) \right] \quad (3.18)$$

The coefficients  $\alpha$  and  $\beta$  are constants defined as 5/9 and 0.09 respectively.

### 3.2.2 LES model

The Large Eddy Simulation (LES) model was proposed in 1963 by Smagorinsky[44]. The main idea of the LES model is to reduce computational cost by ignoring the smallest length scales with a low-pass filtering in the Navier-Stokes equations. The LES model solves THE large-scale fluctuating motions and uses “sub-grid” scale turbulence models for the small-scale motions [43]. Such model is an anisotropic model, mainly applied to the large scales, since the small scales are thought to be isotropic.

The governing equations for the LES model are obtained by filtering the time-dependent Navier-Stokes equations in the physical space. The filtering process, filters out the eddies whose scales are smaller than the mesh spacing or the filter width. The filtered variable is represented with an overbar as shown in the equation (3.20).

$$\overline{\Phi}(x) = \int_D \Phi(x') G(x; x') dx' \quad (3.19)$$

where D is the fluid domain and G is the filter function an is expressed as:

$$G(x; x') = \begin{cases} 1/V, & x' \in V \\ 0 & \end{cases} \quad (3.20)$$

V as the volume control.

### 3.2.3 DES-SST model

The DES model is a hybrid model that combines features of RANS and LES formulations, proposed by Spalart Allmaras, based on a previous set up

blending function. It is based on the idea of using Reynolds Averaged Navier-Stokes formulation (RANS) in attached and mildly separated boundary layers, switching to the use of Large Eddy Simulation (LES) in wall separated regions.

When the DES-SST model is applied the overbar has different meanings to the RANS and LES formulations. For the regions those respond to the URANS formulation (*k-w* SST model), the overbar represents the time average of the quantity and the  $\tau_{ij}$  represents the Reynolds stress tensor.

On the other hand, for the regions where LES model is applied, the overbar indicates a spatial averaging which gives a filtered variable. The  $\tau_{ij}$  represents the sub-grid scale stress tensor (*SGS stress tensor*) that can determine the dynamical coupling between large and small scales in turbulence. Unlike Reynolds stress tensor, the SGS stress tensor is a fluctuating turbulence quantity. The equations (3.21) and (3.22) presents the calculation of  $\tau_{ij}$  for the Reynolds stress tensor and the SGS stress tensor respectively. Only the deviatoric part of the SGS stress tensor is modeled using a statistical approach similar to RANS. The turbulent scales larger than the grid size are directly solved whereas the effects of the SGS scales are modeled, assuming that these scales are more homogeneous in behavior[28]. The equation (3.23) presents the turbulent heat flux in the LES model.

$$\frac{\partial \tau_{ij}}{\partial x_i} = \rho \frac{\partial \overline{u_i u_j}}{\partial x_j} \quad (3.21)$$

$$\tau_{ij} = \overline{\rho u_i u_j} - \overline{\rho u_i} \overline{u_j} \quad (3.22)$$

$$q_j'' = \overline{\rho} (\overline{T u_j} - \overline{T} \overline{u_j}) \quad (3.23)$$

The Reynolds stress tensor in equation (3.21) represents the momentum transfer due to velocity fluctuations. This tensor is symmetrical and is an additional unknown variable in the problem that appears due to the effects of the instantaneous flow that are not present in the mean average flow. This leads to an indeterminate system, because the number of equations is not enough to solve the set of unknown variables.

Boussinesq introduced the first solution for this problem, but for incompressible cases, the equation proposed resulted in the turbulent kinetic energy being zero, which is not true. Kolmogorov in 1941, then, modified the

equation to solve this problem by adding a kinetic as shown in the following equation.

$$-\overline{\rho u_i' u_j'} = \mu_t \left( \frac{\partial \bar{u}_i}{\partial x_j} + \frac{\partial \bar{u}_j}{\partial x_i} \right) - \frac{2}{3} \rho \delta_{ij} k_t \quad (3.24)$$

The switching between the regions solved with each model is made using the idea of the DES model proposed by Strelets[45]. The main idea is switching between the regions where the turbulent length  $L_t$  is lower than the local grid spacing in any of its directions, in these cases the URANS model is then activated. On the other hand, if the turbulent length  $L_t$  is greater than the local grid size, the LES model is rescued.

The turbulent length  $L_t$  is calculated as a function of the turbulent kinetic energy  $k$  and the turbulent eddy frequency  $\omega$ , applying IN the equation (3.25). When the LES mode is activated, the quantity  $L_t$  is replaced by  $C_{DES}\Delta_{max}$ , where  $\Delta_{max}$  is the maximum edge size of the computational domain in any direction.

$$\beta^* k_t \omega = \frac{k_t^{\frac{3}{2}}}{L_t} \rightarrow L_t = \frac{\sqrt{k_t}}{\beta^* \omega} \quad (3.25)$$

The modification made by Stretlets[45] included an additional term, a multiplier ( $\beta k_t \omega$ ) as the destruction term of the turbulent kinetic energy equation  $k_t$ , where  $\varepsilon$  represents the turbulence eddy dissipation and  $F_{DES}$  is the switching function.

$$\varepsilon = \beta^* k_t \omega F_{DES} \quad (3.26)$$

$$F_{DES} = \max\left(\frac{L_t}{C_{DES}\Delta}, 1\right) \rightarrow C_{DES} = 0,61 \quad (3.27)$$

ANSYS® - CFX gives the option of a zonal formulation of the DES model based on the blending functions of the SST model. When  $F_{SST}$  is set as zero, the Strelets model is applied [45].

$$F_{DES-CFX} = \max\left(\frac{L_t}{C_{DES}\Delta}(1 - F_{SST}), 1\right) \rightarrow F_{SST} = 0, F_1, F_2 \quad (3.28)$$

### 3.3 Forced convection heat transfer

The forced convection is characterized by the fluid being forced to flow over a surface, driven by a pump or a fan. Convection heat transfer can be complicated because it involves fluid motion and also heat conduction, but despite the complexity of convection, the rate of heat transfer in this mechanism is proportional to the temperature difference and is expressed by Newton's Law of cooling[46].

$$q'' = h(T_s - T_\infty) \quad (3.29)$$

Where,

$q''$  = Heat flux [ $W/m^2$ ]

$h$  = Convection heat transfer coefficient [ $W/m^2K$ ]

$T_s$  = Temperature of the surface [ $K$ ]

$T_\infty$  = Temperature of the fluid sufficiently far from the surface [ $K$ ]

#### 3.3.1 Nusselt number

The Nusselt number is a dimensionless number that measures the increase of heat transmission, from the surface on which a fluid flows by convection compared to the transfer of heat if it occurs only by molecular diffusion. In the equation (3.30),  $L_c$  is a characteristic length of the problem. For complex shapes it may be defined as the volume of the body divided by its surface. The thermal conductivity of the fluid is assigned by  $k$ .

$$Nu = \frac{hL_c}{k} \quad (3.30)$$

#### 3.3.2 Heat transfer in concentric channels

There are many studies that deals with the problem of heat transfer in concentric annuli, but only after the work developed by Gnielinski[11], the diameter ratio was included in an analytical expression to calculate values as the friction factor  $f$  and Nusselt number, NU. Besides the  $D_i/D_o$  ratio, other factors as Reynolds number, Prandtl number and thermal boundary conditions for the walls were also taking into account, as seen in equations (3.32) to (3.34).

The Reynolds number is a dimensionless number that allows characterizing the flow regime. Its value indicates whether the flow follows

under laminar or turbulent regime, as shown in equation (3.31). Where  $L_c$  is the characteristic length, in our case, the hydraulic diameter,  $D_h$ . The analytical solution written by Gnielinski[11], proposed a correction in the Reynolds number that considers the diameter ratio of the channel, implying in a mean velocity and the friction factor.

$$\text{Re} = \frac{\rho u L_c}{\mu} = \frac{u L_c}{\nu} \quad (3.31)$$

$$f_{ann} = (1.8 \log_{10} \text{Re}^* - 1.5)^{-2} \quad (3.32)$$

$$\text{Re}^* = \text{Re} \frac{(1+a^2) \ln a + (1-a^2)}{(1-a)^2 \ln a} \quad (3.33)$$

$$a = \frac{D_i}{D_o} \quad (3.34)$$

The Nusselt number for forced convective heat transfer is commonly expressed as a function of two principal parameters, the Reynolds number and the Prandtl number. The Prandtl number is defined as the momentum diffusivity and thermal diffusivity ratio as shown in equation (3.35). In the case of the expression developed by Gnielinski[11], besides these two numbers, other parameters have been taken into account to predict the Nusselt values. The variation of fluid properties, represented as a constant,  $K$  varies for each thermal boundary condition, the equation (3.37) presents the calculation of  $K$  for the case of heating gas. The factor  $k_1$  and the factor  $F_{ann}$ . The last one depends on the thermal boundary condition. If the thermal condition is heat transfer at the inner wall and the outer wall insulated, the factor  $F_{ann}$  assumes different value in comparison to the case which the inner wall is insulated and the outer wall heated.

$$\text{Pr} = \frac{\nu}{\alpha} = \frac{\mu/\rho}{k/(c_p\rho)} = \frac{c_p\mu}{k} \quad (3.35)$$

$$\text{Nu} = \frac{(f_{ann}/8)\text{Re Pr}}{k_1 + 12.7\sqrt{f_{ann}/8}(\text{Pr}^{2/3}-1)} \left[ 1 + \left( \frac{D_h}{L} \right)^{2/3} \right] F_{ann} K \quad (3.36)$$

$$K = \left( \frac{T_\infty}{T_s} \right)^n \rightarrow n = 0.45 \quad (3.37)$$

$$k_1 = 1.07 + \frac{900}{\text{Re}} - \frac{0.63}{(1+10\text{Pr})} \quad (3.38)$$

$$F_{ann} = (0.9 - 0.15a^{0.6}) \quad (3.39)$$

### 3.3.3 Heat transfer in eccentric channels

In the case of eccentric channels, the calculations of the heat flux and the Nusselt number are made using the equations (3.29) and (3.30) respectively. The equation (3.29) can be rewritten in terms of the bulk temperature in the cross section,  $T_b$ , rather than  $T_\infty$ . The bulk temperature is defined as the ratio between the rate of flow enthalpy through a cross section and the rate of flow of heat capacity through a cross section[47]. The equation (3.40) shows the expression for the case with constant heat flux.

$$T_b = \frac{1}{uA} \int_0^A uT dA \quad (3.40)$$

Chang and Tavoularis[37] studied the heat transfer process in a rectangular channel with an inner rod. To obtain the surface temperature of the rod, they presented the equation (3.41). Taking into account the axial and azimuthal directions and the temperature of the surface in each point.

$$T_r(x,t) = \frac{1}{2\pi} \int_0^{2\pi} T_{rod}(x,\phi,t) d\phi \quad (3.41)$$

## 4 METHODOLOGY

### 4.1 Computational domain and mesh

The first simulation presented in this work was carried out in the same computational domain, geometric parameters and Reynolds number used by Choueiri and Tavoularis[1] in their experimental work. The channel is composed by an external tube with an outer diameter of  $D_o = 50.8$  mm and a core tube (inner diameter) with  $D_i = 25.1$  mm, leading to a diameter ratio of approximately 0.5. The hydraulic diameter, used in calculations of non-circular passages is defined as a cross-sectional area and the wetted perimeter ratio, shown in equation (4.1). So, the hydraulic diameter is then computed as  $D_h=25.7$  mm. The tube has an eccentricity of 0.8 and a total length of 1500 mm. The eccentricity is calculated as shown in equation (4.2) with  $\Delta y$  as the distance between centers. After the first simulation new computations were carried out varying the eccentricity between 0.7 and 0.9 in intervals of 0.05 maintaining all the other geometric parameters used by Choueiri and Tavoularis [1] in their experimental work.

$$D_h = \frac{4A}{P} \quad (4.1)$$

$$e = \frac{2\Delta y}{D_o - D_i} \quad (4.2)$$

The origin of the cartesian coordinates is located in the center of the outer diameter and in the beginning of the channel, with the flow flowing in the parallel to x-axis, from the left to the right, Figure 4.1. The spanwise direction of the flow coincides with the z-axis and the y-axis is in the vertical direction.

To build the mesh, special care was taken near the wall. At such region a small size mesh were built to capture the different characteristics of the boundary layer. The  $y^+$  used near the walls was maintained less than 0.5, as shown in Table 4.1, regardless the eccentricity. In the streamwise direction of the domain 300 equidistant points were used, which produced a cell size of 6 mm. The coarsest cell in the transversal section is always smaller than the cells in streamwise direction.

The total number of nodes for all the cases was 1224120, the number of elements 1200000 and the number of faces 48000.

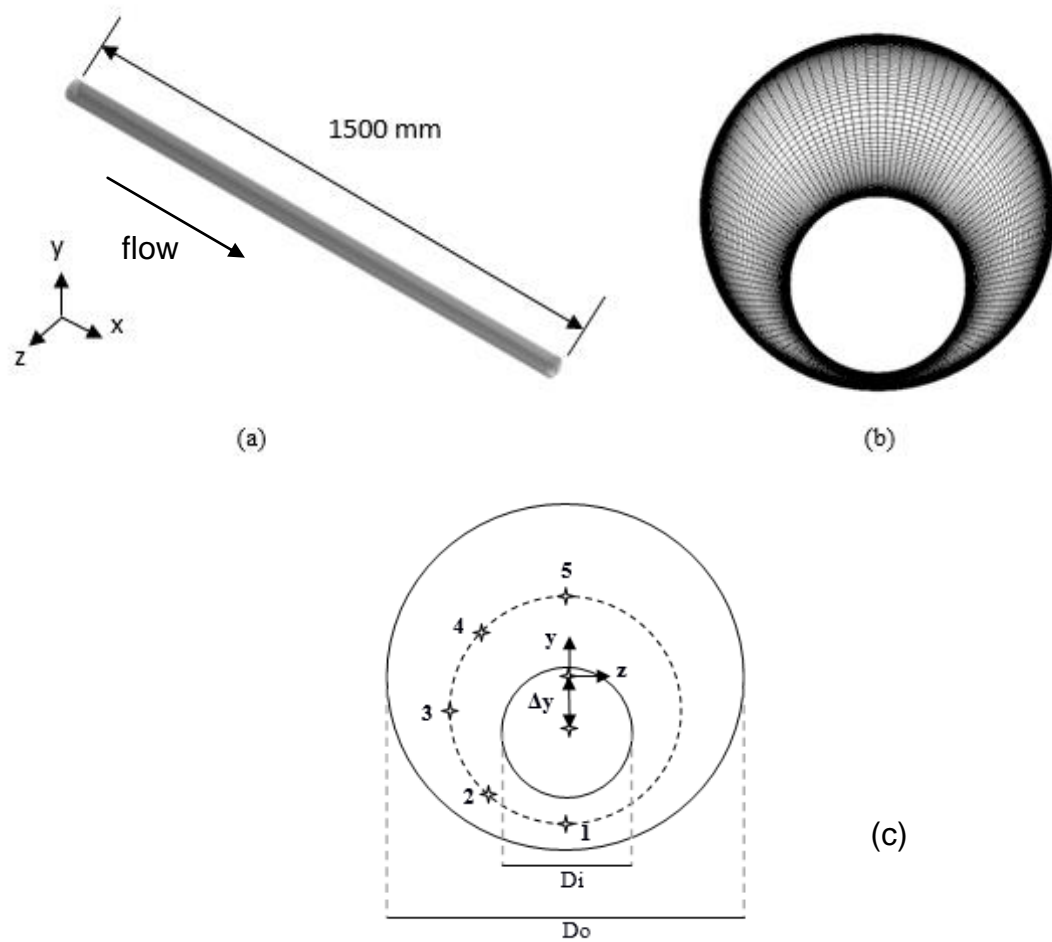


Figure 4.1 Computational domain. (a) Schematic view of the channel. (b) Mesh of the cross section. (c) Cross-section of the channel.

Table 4.1 Distance of the first element near the wall in all the cases

Eccentricity	Distance of the first element [m]
0	1.0e-5
0.7	3.0e-6
0.75	2.5e-6
0.8	2.0e-6
0.85	1.5e-6
0.9	2.9e-6

In order to compare the numerical results with the experimental outcomes from Choueiri and Tavoularis[1] it will be analyzed the same five

points in the cross-section that the authors did, as shown in the Figure 4.1. The points (1 up to 5) lies on the line that describes the middle path between both inner and outer walls. The Table 4.2 presents the z and y coordinates of each point in the cross-section of the annular channel.

Table 4.2 Coordinates of the measurement points for the experimental case

Point	Z	Y
1	0	-0.024384
2	0.013716	-0.018796
3	0.019304	-0.00508
4	0.013716	0.008636
5	0	0.014224

## 4.2 Boundary conditions

The boundary conditions used for all the simulations either concentric or eccentric annuli were the following.

### 4.2.1 Isothermal case

The boundary conditions adopted for the isothermal case are presented in the Figure 4.2. The inlet velocity was setted as 9.0183 [m/s] to obtain a Reynolds number of 15000. The turbulence intensity was chosen 5% in the inlet and the outlet condition established was a differential pressure of 0 [Pa]. Both inner and outer walls were set as smooth wall with no slip condition.

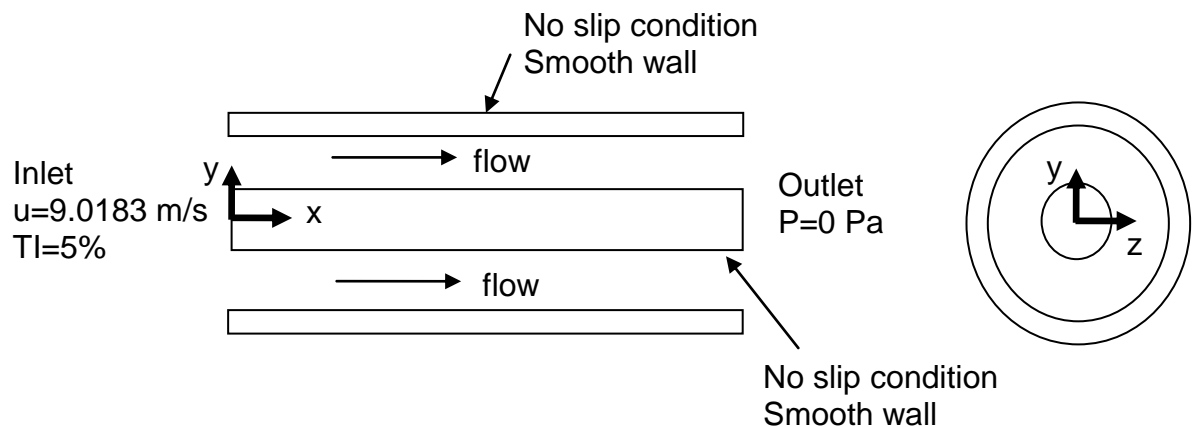


Figure 4.2 Boundary conditions of the isothermal case

#### 4.2.2 Heat transfer case

Figure 4.3 presents the boundary conditions used for the simulations of the non-isothermal computations for both concentric and eccentric cases. Similarly to the isothermal case showed in Figure 4.2, the inlet velocity, turbulence intensity and conditions for the outer wall were maintained. At the channel's inlet temperature was set 298 [K]. At the channel's outlet opening condition was applied with an outlet temperature of 313 [K]. The flow cross through the channel just one time, the translational periodicity condition for any of the simulations was not applied.

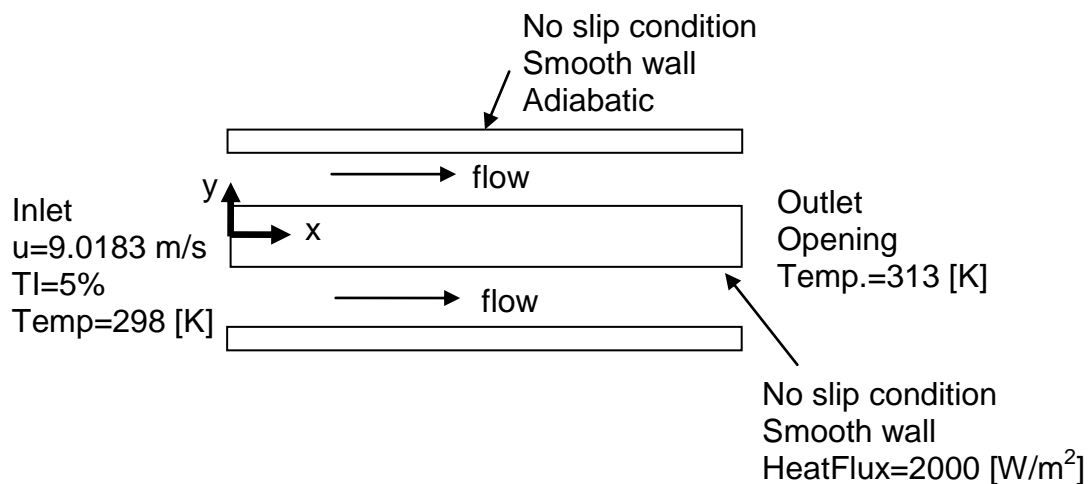


Figure 4.3 - Boundary conditions of the non-isothermal case

A prescribed heat flux of 2000 [W/m<sup>2</sup>] was set on the inner wall's surface.

For the outer wall a no slip condition, smooth wall and adiabatic condition was setted.

It is important to highlight that for both cases with and without heat transfer process, the time step for all simulations was chosen taking special care in guarantee a Courant number lower than 1. The time step was maintained constant for each simulation. The table below summarizes the time step setted and the numer of time steps simulated for each case.

Case	Time step	Number of time steps
REF	1.4e-4	17957
A	1.0e-4	23505
B	1.0e-4	21655
C	9.0e-5	38217
D	8.0e-5	17413
E	1.5e-4	17556

### 4.3 Turbulence Settings – DES-SST

In the section 3.2 we explained the formulation of the DES-SST model. In this simulation the shielding function of the SST blending was used, applying the formulation of the equation (3.2), the blending factor was chosen as 0 and the  $C_{DES}$  remained with a value of 0.61.

The transient scheme which defines the discretization algorithm for the transient term was chosen Second Order Backward Euler. For the advection scheme was selected central difference with the activated option of bounded CDS which is highly recommended in cases using DES and SAS models due to the control of the courant number between the specified advection scheme and the central difference scheme (CDS) [43].

### 4.4 Simulations performed

The main goal of the present work is to validate the behavior of a developing turbulent flow in an eccentric channel and study the influence of the velocity fluctuations in the heat transfer coefficients. In order to achieve this main purpose, it was decided to start from the geometry used in the experimental work of Choueiri and Tavoularis[1]. Once we have the experimental results from the authors, it was possible to validate the results obtained from the numerical simulation for a pure dynamic eccentric case,  $e=0.8$ .

As mentioned before there are currently no analytical equations to solve the heat transfer problem in eccentric channels under turbulent flow. That is the reason why the methodology, mesh, boundary conditions and turbulence model needed to be tested and to be compared with the experimental results for the pure dynamic eccentric case. In sequence it will be possible to use the same

methodology and conditions for the cases where the heat transfer process was added.

For this purpose, a concentric channel with the same diameter ratio and a Reynolds number of 15000, was first simulated. Constant heat flux of 2000 [W/m<sup>2</sup>] in the inner wall and insulated outer wall was imposed. The numerical results were compared with the analytical equations from Gnielinski[11](equations (3.31) to (3.39)). After the validation of the methodology the same parameters were applied to the eccentric cases.

In order to give initial values for the transient simulation, RANS K- $\omega$  SST was set up and running in steady state. After complete these simulations, the transient cases were then initiated. In all cases the maximum Courant number was maintained between 0.8 and 0.9. The total time of simulation was large enough to provide approximately 15 flow-through or convective time. The convective time is defined as the time that takes to the fluid flow from the beginning to the channel until the end.

All the simulations were performed in a computer Intel Quad-core i7 7700k processor, RAM memory of 32 Gb, using as operating system Windows 10 Home and a GTX 1050 Ti video card. The physical time of each simulation was about 2 weeks for each simulation.

## 5 RESULTS AND DISCUSSION

In this chapter the results obtained from the numerical simulations for the channel with the same parameters used by Choueiri and Tavoularis[1] will be presented. After validating and comparing both, experimental and numerical results, the non-isothermal eccentric cases will be presented. Table 5.1 shows the denominations that will be used as reference for each one of the eccentricities simulated in this work. The concentric case will be used as a reference for non-isothermal cases.

Table 5.1 Denomination of the different eccentricity cases.

<b>Eccentricity</b>	0	0.7	0.75	0.8	0.85	0.9
<b>Case</b>	REF	A	B	C	D	E

### 5.1 Isothermal eccentric channel

#### 5.1.1 Mean flow development

To validate the flow simulation in the eccentric channel measurements of the three velocity components and its respective mean average values were taken at the five positions shown in Figure 4.1(c). The development of the velocities along the channel are presented in Figure 5.1 at 5 seconds of simulation. The points measured are the same as the ones chosen by Choueiri and Tavoularis[1]. It should be remembered that the z-axis corresponds to the spanwise direction, this means that the  $u$  and  $w$  velocity components will be representing the streamwise and spanwise directions respectively.

In the case of the spanwise velocity, that coincides with the z-axis and the  $w$  velocity, the local mean velocity is null,  $w/u_b=0$ , regardless the point where the velocity data was gathered. Besides that, the flow fluctuations start more or less at  $x / D_h = 30$ .

Two kinds of behavior are observed in the streamwise velocity. In the points 1 and 2 a peak of velocity is around  $1.2u_b$ , being such value noticed in the beginning of the channel. Going farther towards the channel's outlet, at

$x / D_h = 20$ , the ratio of velocities decrease to  $0.15u_b$  in point 1 and  $0.6u_b$  in the point 2. This interval between  $0 < x / D_h < 20$  is defined as the entrance region ER. From  $20 < x / D_h < 40$  (as the fluctuation growth region, FG) there is an increase of the mean velocity and the fluctuations start to appear around  $x / D_h = 30$ , from this zone to the end of the channel, is the rapid mixing region, RM. At this region is possible to see the establishment of the mean velocities and fluctuations. The names of the regions were proposed by Choueiri and Tavoularis [1] and the behavior of the flow described by them in each one of the regions were found in the numerical simulation.

For the points 3, 4 and 5, the pattern in the first two regions it is different from the points 1 and 2. Unlike the first two cases, at  $0 < x / D_h < 20$ , there is an increase of the mean velocity. However, point 3 reach the maximum velocity first in comparison with points 4 and 5. Afterwards, a slightly velocity decrease takes part continuing up to the next region before the establishment of the mean value and the fluctuations. A similar behavior was also observed by Chang and Tavoularis [37] at the narrow gap in a rectangular channel with a cylinder inside.

The three regions mentioned above and the behavior presented in each point for velocity, matches with the experimental results encountered by Choueiri and Tavoularis[1]. They defined this regions as entrance region, ER from  $0 < x / D_h < 20$ , fluctuations growth region, FG  $20 < x / D_h < 40$  and rapid mixing region, RM  $40 < x / D_h < 60$ . These definitions are going o be used in the present work.

Although in all positions the three main regions proposed by Choueiri and Tavoularis [1] are identified, the point 1 located at the narrow gap will be object of the main dynamical analysis.

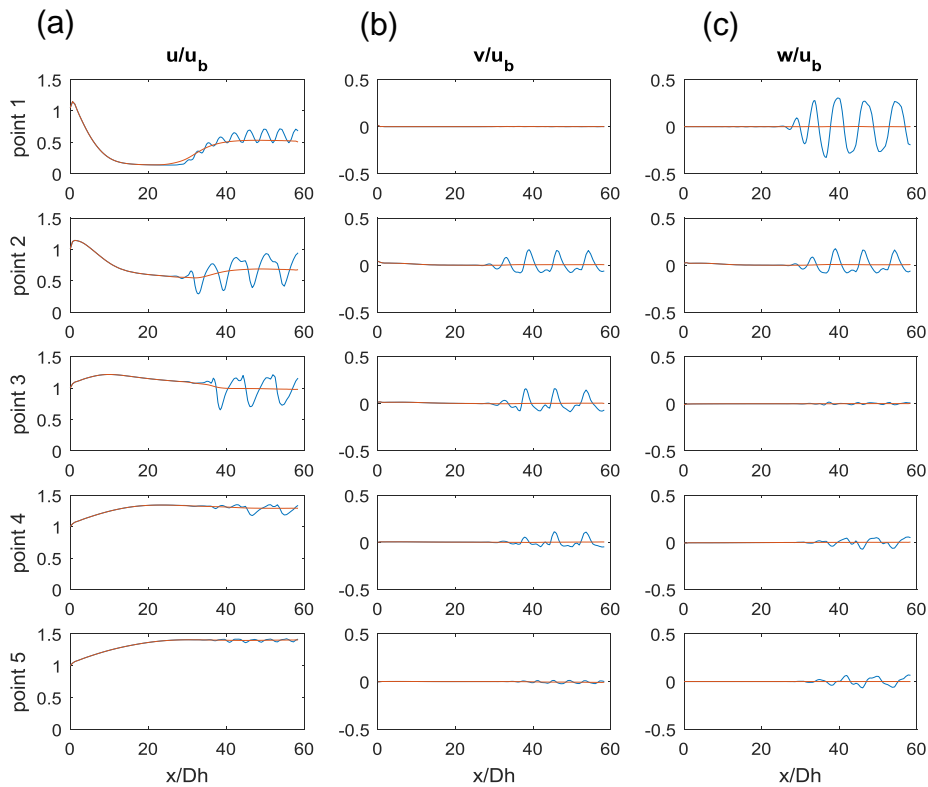


Figure 5.1 Velocity fluctuations of the main components, the blue line represents the velocity fluctuations along the channel and the red line the mean average velocity. (a) Streamwise direction. (b) vertical-velocity component. (c) Spanwise direction.

The Figure 5.2 presents the behavior of the three velocity components obtained experimentally by Choueiri and Tavoularis[1]. It is possible to see that the patterns as well as the magnitude of the mean velocity in each component assigned to each point are in good agreement with the numerical simulation performed in this work and presented by Figure 5.1. This agreement with the experimental outcomes, enable us to conclude that that the conditions established for the simulations are able to predict the dynamical behavior with a good accuracy.

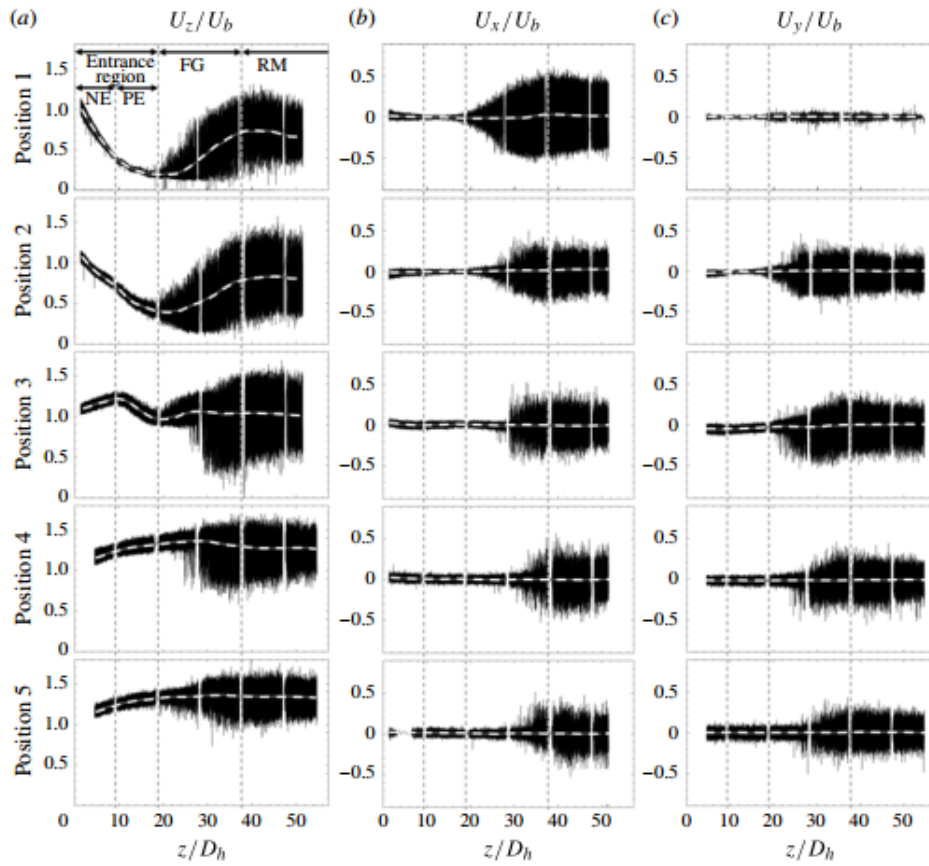


Figure 5.2 Velocity fluctuations of the three main components at five measurement points obtained experimentally by Choueiri and Tavoularis[1]. (a) Streamwise fluctuations ( $z$  axis). (b) Spanwise fluctuation at the measurement points ( $x$  axis). (c) Velocity fluctuations in the  $w$  direction ( $y$  axis).

### 5.1.2 The dynamics of the flow – the strouhal for isothermal flow

The Strouhal number  $St$  allows to adimensionalize the frequency using the macro scales of the problem and it is defined as:

$$St = \frac{fD_h}{u_b} \quad (5.1)$$

The streamwise and spanwise velocities time-traces for the three main regions are shown in Figure 5.3. Data were gathered at point 1 of the Table 4.2 corresponding to the narrow gap for  $x/D_h = 38, 42$  and  $53$ . The points are chosen at the end of the FG region, at the beginning of the RM region and near the outlet of the RM region. The reason why the points are gathered in these points is because an the end of the FG region an along the RM region, the flow reach an stable oscillation.

In the streamwise direction, AT  $x/D_h=38$ , the fluctuations does not have a stable mean value during the time, on the other hand, for the positions at  $x/D_h=42$  and  $x/D_h=53$  the velocity fluctuates around approximately  $0.56u_b$  and  $0.6u_b$  respectively.

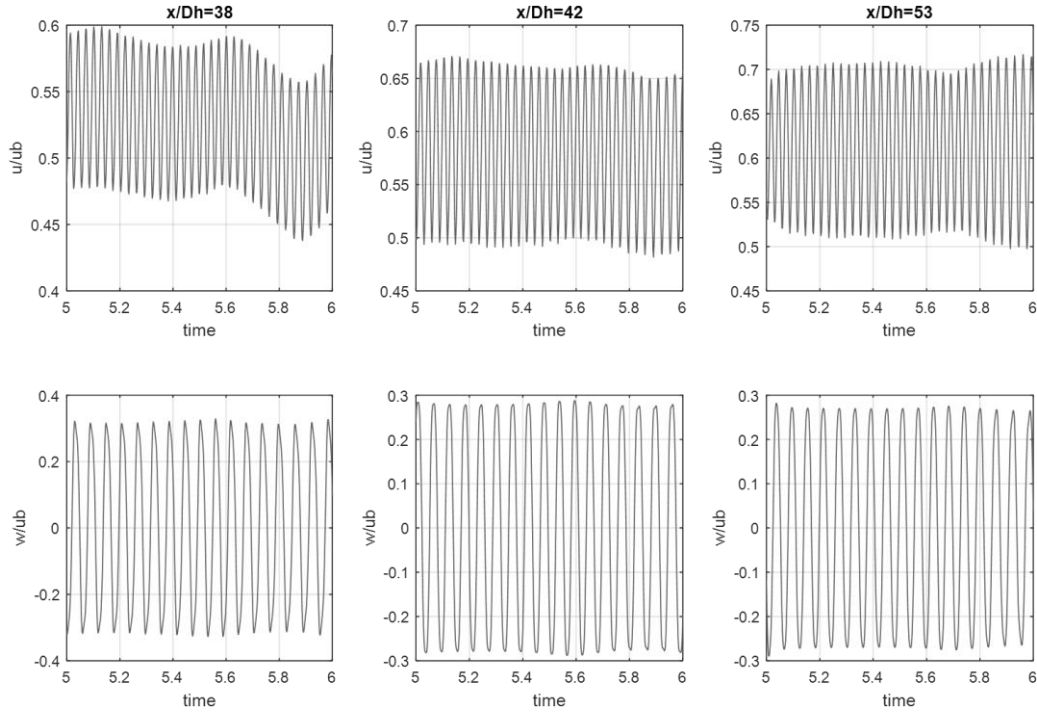


Figure 5.3 Streamwise and spanwise velocity fluctuations at five seconds of simulation for the point 1 located at the narrow gap. (a)  $x/D_h=38$ , end of the FG region. (b)  $x/D_h=42$ , beginning of the RM region. (c)  $x/D_h=53$ , end of the RM region.

In order to obtain the frequency of the oscillations of the signal, a Fast Fourier Transform (FFT) was used. The fundamental frequency of the oscillatory motion in the streamwise velocity component was approximately twice the frequency of the one found in the spanwise direction. Applying equation (5.1) the value of the Strouhal number for both components in each region (ER, FG, RM) is then obtained. The results are presented in Figure 5.4.

Due to the difference between the properties of the fluid used for the experimental case and the simulations, in order to maintain the same Reynolds number, the velocity in the numerical case is 10 times higher compared with the experimental case. Therefore, the frequencies obtained are also 10 times higher than the ones obtained by Choueiri and Tavoularis[1]. Even so, the values obtained for the Strouhal number of 0.2 and 0.1 for the streamwise and

spawise velocities components respectively, agrees with the experimental results obtained by their experimental campaigning.

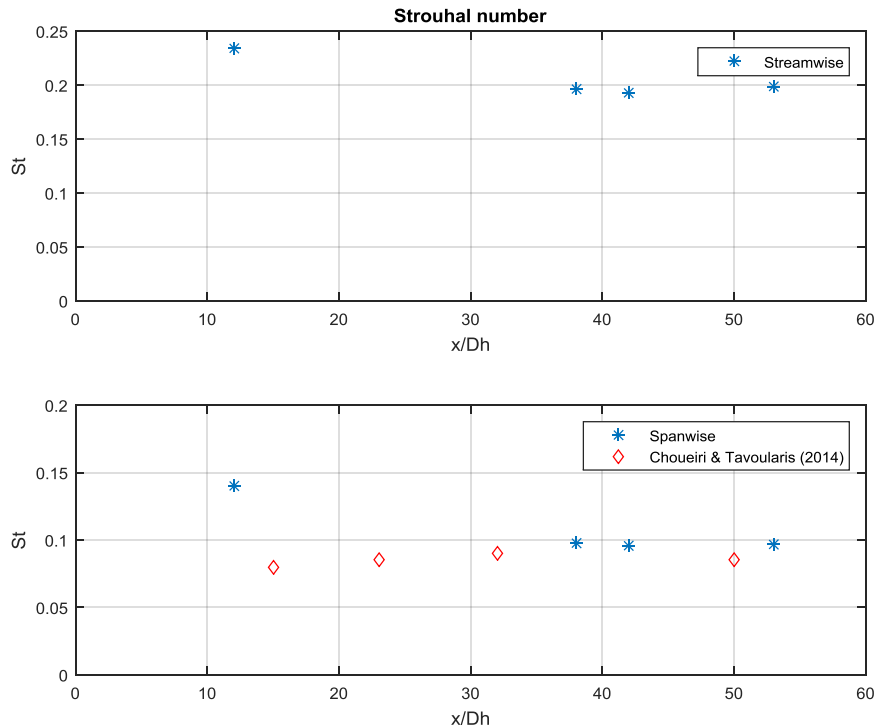


Figure 5.4 Strouhal number along the channel's length, in the narrow gap

## 5.2 Non-isothermal cases

In this section will be analyzed the mean average and fluctuant field of the flow under the same fluid dynamic boundary condition, but adding different eccentricities. Besides the changes adopted in face of the new eccentricities we also coupled the problem imposing prescribed heat transfer boundary conditions on the tube's surfaces. Each eccentric case will be compared with a concentric one simulated under the same boundary conditions. As mentioned before analytical expressions are provided for Gnielinski [11] that allow us to validate the numerical results only for the concentric case.

### 5.2.1 Main velocity components in the narrow gap

Figure 5.5 shows the behavior of the mean average velocity in the streamwise direction for the concentric case in the narrow gap (presented as a solid line). Each eccentric case simulated is also showed. The eccentricity was ranged from 0.7 up to 0.9. The concentric case has a value of approximately  $1.15 u_b$  and, as expected, there is not velocity fluctuations for any farther station

along the channel. For the case A, corresponding to an eccentricity of 0.7, the mean velocity decreases to 37% compared with the concentric channel as a consequence of the area reduction inside the narrow gap.

As the eccentricity increases, the station where the flow field starts to present the quasi-periodic motion, moves toward to the channel's inlet. It means, the onset of the gap instabilities has shortened with the eccentricity increasing. For the eccentricity of 0.75 the velocity fluctuations start almost at the end of the channel at  $x/D_h=52.5$ , whereas for the eccentricity of 0.9 the velocity fluctuations are noticed soon after the channel's entrance at  $x/D_h=8.3$ .

As the inner tube goes closer to the outer one, the eccentricity increases and the gap become narrower. The gap reduction will produce a reduction in the mean velocity at this point, since the viscosity dominates the flow inside the tight gap. It is important to notice that when the velocity fluctuations appear, they cause an increase in the mean velocity. For all studied cases the velocity is not enough to reach the same value of the velocity obtained for the reference case ( $e=0$ ). But it is noticeable that the presence of the velocity fluctuations can increase the mean velocity value.

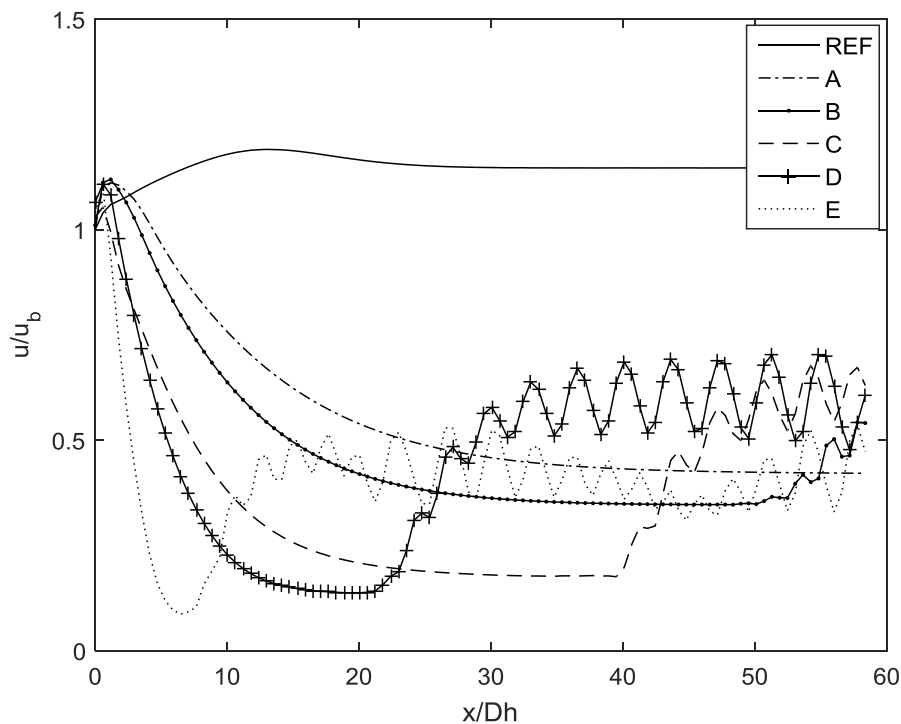


Figure 5.5 Comparisson of the streamwise velocity  $u_m/u_b$  along the channel

Figure 5.6 shows the fluctuations of the spanwise velocity along the channel. There is no velocity fluctuations along the gap for the reference case and the case A, ( $e=0.7$ ). For the other cases the spanwise velocity fluctuates around 0 between -0,3 and 0.3. This amplitude is almost the same in cases B, C, D and E, the difference between these cases is the onset of the velocity fluctuations that is directly influenced by the eccentricity. These fluctuations proves that there are coherent structures crossing the gap between the subchannels located at each side of the narrow gap.

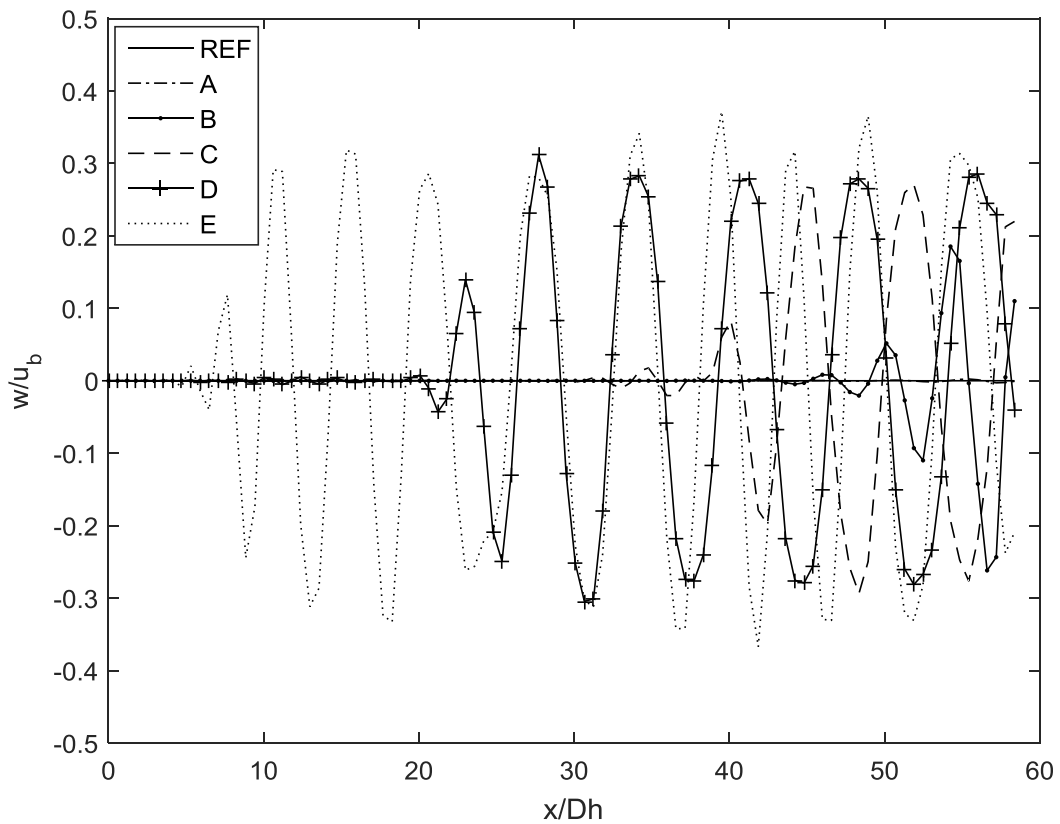


Figure 5.6 Comparisson of the spanwise velocity  $w_m/u_b$  along the channel inside the narrow gap.

### 5.2.2 Velocity contours and profiles

In Figure 5.7 (a) - (f) the contour plots of the mean average streamwise velocity component are shown for every simulated channel at  $x/D_h=50$ . The isolines of the mean average velocities are made dimensionless by using the bulk velocity. Due to the good symmetry only the half part of the picture is

shown. First of all, it is noticeable the great symmetry of the flow, regardless the eccentricity of the channel.

As expected in the eccentric cases the velocity reach a maximum value in the wider gap. On the other hand the minimum velocity appears in the narrow one. In cases A and B, which did not present velocity fluctuations, or only appeared at the end of the channel, the narrow gap presents a minimum velocity of approximately  $0.4u_b$ . In the cases C and D, despite the gap reduction, through the eccentricity increasing, the flow velocity inside it was found to be higher (around  $0.6u_b$ ) in comparison with the cases A and B, being such behavior attributed to the velocity fluctuations that seems to play an important role on the mass distribution inside the channel. This kind of mass distribution and the velocity increasing with the fluctuating field was also reported by Lee and Barrow [30]. This behavior is in agreement with the one found in Figure 5.5. The onset of the gap instabilities in cases C, D and E, assigned by the velocity fluctuations, lead to a streamwise velocity increasing inside the narrow gap in comparison with cases A and B.

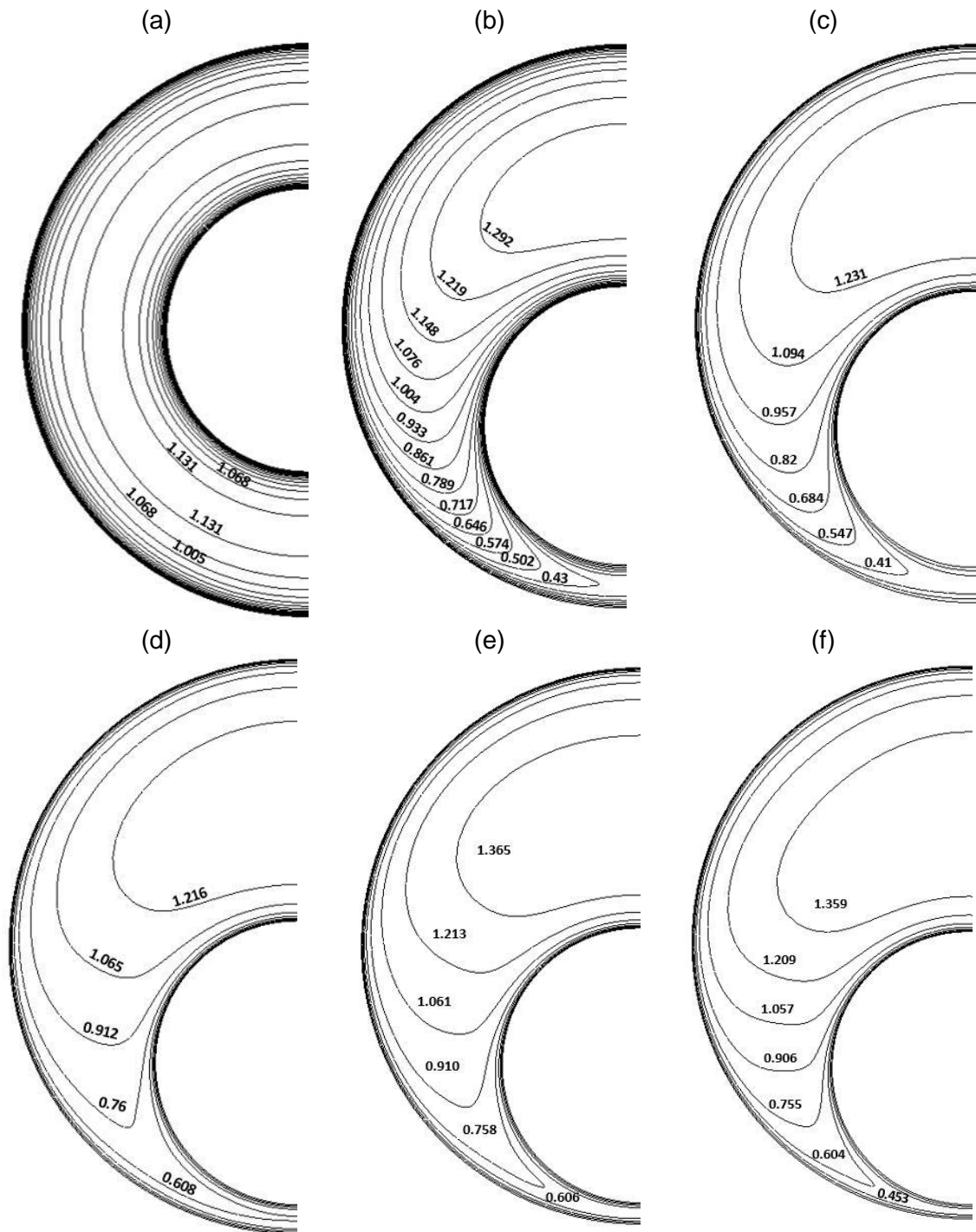


Figure 5.7 Velocity contours of the streamwise velocity component in the transversal plane located at  $x/D_h=50$ . (a) Reference case. (b) Case A. (c) Case B. (d) Case C. (e) Case D. (f) Case E.

The Figure 5.8 presents the velocity profiles in the narrow gap for all the studied cases at different streamwise stations,  $x/D_h$ , along the channel. The velocity is presented in non-dimensional form by using the bulk velocity,  $U_b$ . The non-dimensional velocity is stressed as a position function, also made

dimensionless by the gap size  $S$ . Figure 5.8 (a) shows the reference case corresponding to a concentric channel. The velocity profile has a flattened shape in the center of the gap that is characteristic of a turbulent flow near solids surfaces, seemingly to be independent of the streamwise position along the channel. The flattened shape obtained in the velocity profile was found in previous works [3][7][18][19][24]. Moreover, the maximum velocity reach an approximate value of  $1.2u_b$ .

Looking at the Figure 5.8 (b) and (c), that correspond to the cases A and B, the eccentricity is not high enough to produce fluctuations in the velocity field, therefore, at the interior of the channel there is a reduction of the velocity around 35% and 54.5% respectively compared with the reference case. As we move further, from the inlet of the channel, the velocity decreases until reaching a value of  $0.42u_b$  for the case A and  $0.38u_b$  for the case B which is expected as a consequence of the width gap reduction as the eccentricity increases. It is important to notice in the case B that although the velocity fluctuations exist (even nearby the end of the channel), their influence in the velocity profile is not evidenced by the isolines of velocity distribution, as shown in Figure 5.7 and Figure 5.8.

In Figure 5.8 (d) is presented the case C ( $e=0.8$ ). This is the first case in which the velocity fluctuations appear, reaching a stable behavior oscillating around a constant value. The solid line corresponding to the position  $x/D_h=10$  still presents a reduction of the velocity with the increasing of the eccentricity ( $0.38u_b$ ) and this reduction continues until  $x/D_h=30$ . In the streamwise station located at  $x/D_h=40$ , where gap instability appear for the very first time, it is possible to see a slight increasing of the values of the velocity profile, about 5 % compared with upstream position at  $x/D_h=30$ . This increasing becomes more evident as we move farther towards the channel's inlet. At  $x/D_h=50$ , where the velocity fluctuates around a constant value, the maximum velocity reaches  $0.69u_b$ . Such value is approximately the same velocity found at the beginning of the channel for the case B.

The increasing of the values of the velocity profile due to the velocity fluctuations is evident in Figure 5.8 (e) and (f). In both figures, from the point of onset of the velocity fluctuations there is always an increasing in the maximum values of the velocity that is evident in the velocity profiles compared with the

profile presented with a solid line which is in a location where there are not fluctuations. Even so, the Figure 5.8 (f) does not shows a higher increasing compared with Figure 5.8 (e). Such fact will be expected since the fluctuations started earlier. This might be attributed to the viscous effects that are higher in the case of very tight gaps. The viscous effects might be also de reason why at stations  $x/D_h=40$  and  $x/D_h=50$ , the velocity profile in Figure 5.8 (f) presents lower values compared with station  $x/D_h=30$ .

In the Figure 5.9 the velocity contours for the case D is shown for different stations downstream the channel. In the same way the data were made non-dimensional through the bulk velocity. In Figure 5.9 (a) it is presented the velocity contours in a region where there is still not velocity fluctuations. The difference between the velocities found in the narrow and the wider gap for this position are around 87%. In Figure 5.9 (b) and (c) located at  $x/D_h=40$  and  $x/D_h=50$  respectively, it is noticed that the maximum velocity increases in both the wider and the narrow gap, this behavior is in concordance with the one found Figure 5.8 (e). From the point where the velocity fluctuations appear, the velocity profile changes and the maximum velocity increases compared to the one found at the beginning of the channel. Station where the velocity fluctuations still does not exist.

It is important to notice that the large area region where the maximum velocity takes place (wider gap) in the Figure 5.9 (a) decreases in the Figure 5.9 (b) and (c), reinforcing the new flow characteristic as the flow evolves inside the channel. This shows that there is a new distribution of the mass from the moment when the velocity starts to fluctuate.

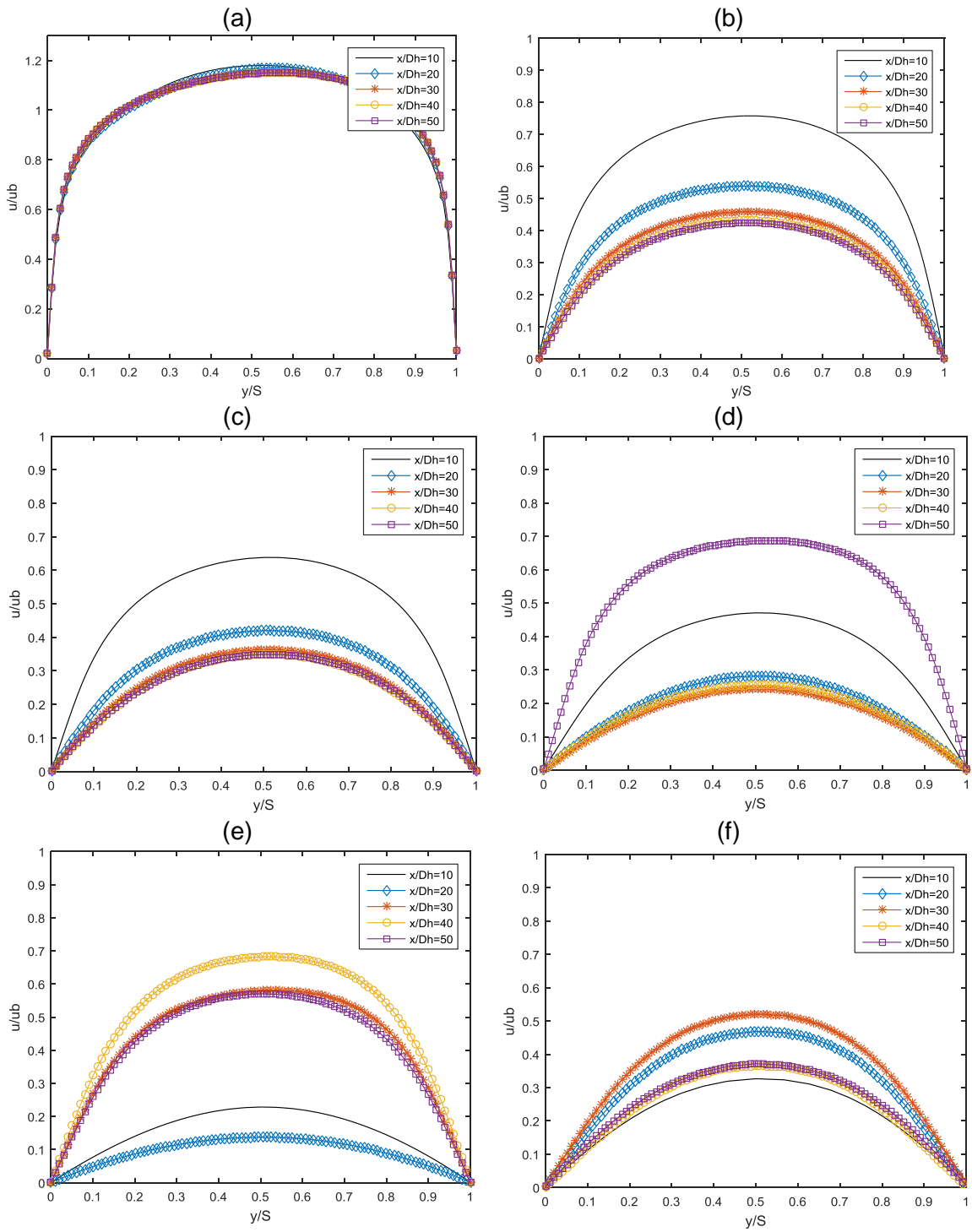


Figure 5.8 Velocity profiles in the narrow gap at different stations along the channel. (a) Reference case. (b) Case A. (c) Case B. (d) Case C. (e) Case D. (f) Case E.

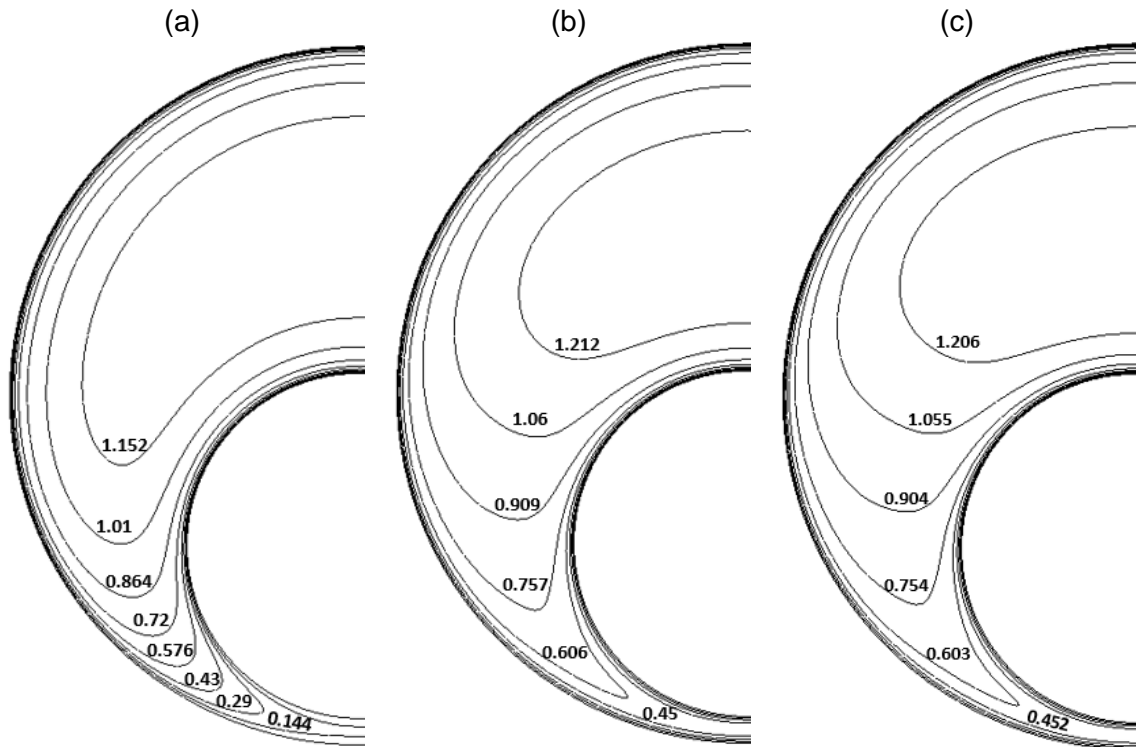


Figure 5.9 Isocontours of the streamwise velocity component for the case D at different stations along the channel's length. (a)  $x/D_h=20$ . (b)  $x/D_h=40$ . (c)  $x/D_h=50$

### 5.2.3 Fluctuation intensities

Figure 5.10 are depicted the intensity of velocity fluctuations in the streamwise direction at  $x/D_h=50$  for each simulated case. The values are displayed in dimensionless form by using the bulk velocity  $u_b$ . All the figures presents symmetry along the vertical axis, so, that is the reason why is presented only the half part of the transversal plane of the channel.

For the reference case, Figure 5.10 (a), the maximum axial velocity intensity is around  $\sqrt{u'^2}/u_b=0.08$ , being found near the inner and outer wall showing a constant distribution in both horizontal or vertical axis. As the eccentricity starts to increase (Figure 5.10 (b) and (c)) the velocity intensities distribution changes and the maximum values are found in regions near to the wider gap reaching values of around  $\sqrt{u'^2}/u_b=0.081$  and the minimum velocity

intensities are found in the narrow gap with values between  $\sqrt{u'^2}/u_b = 0.01$  and  $\sqrt{u'^2}/u_b = 0.03$ .

In Figure 5.10 (d), (e) and (f) the isoline maps of the velocity intensities distribution in the streamwise direction is almost constant. In these cases the velocity fluctuations already exist. It is interesting to notice at  $90^\circ$  is the location at which the maximum value of  $\sqrt{u'^2}/u_b$  is found, being  $0^\circ$  located at the center of the narrow gap in the inner tube. Besides that, the minimum value of the velocity fluctuations, surprisingly, takes place at regions near to the wider gap. Similar behavior was found by Nikitin [8], in his work the author found the maximum values of the velocity intensities taking place nearby  $90^\circ$ . Moreover, his outcomes presented almost the same values in the vicinity regions of the narrow and wider gaps.

Looking at the narrow gap, the intensity velocity fluctuation assumes values lower than found at  $90^\circ$  and higher than we found at the wider gap. This shows that the velocity intensities increase from  $0^\circ$  to a maximum value at  $90^\circ$  and decreases again until its minimum value near to  $180^\circ$ . This behavior was found for cases C, D and E (numerical simulations whose the fluctuating field was prescribed).

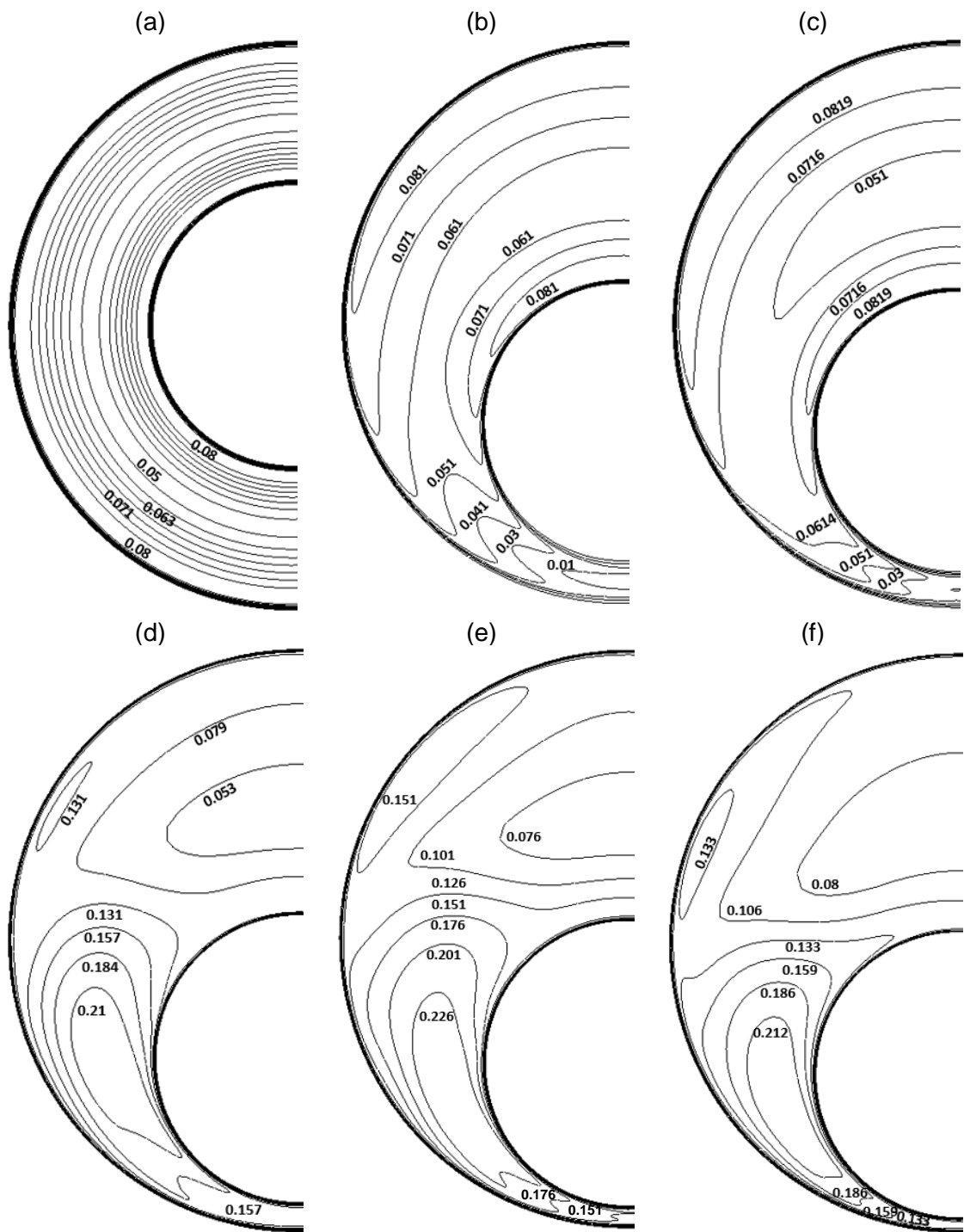


Figure 5.10 Streamwise velocity fluctuation intensity contours of  $\sqrt{u'^2}/u_b$  at  $x/D_h=50$ . (a) Reference Case. (b) Case A. (c) Case B. (d) Case C. (e) Case D. (f) Case E.

As well as the velocity intensities in the streamwise direction, is also important to take a close look in the intensity of the fluctuant spanwise component of the velocity field. In Figure 5.11 the isocontours of these intensities are shown for every simulation, the concentric case and the other five eccentricities cases. The fluctuations in the spanwise direction are also presented in non-dimensional form through the bulk velocity. For the concentric case, the distribution, as expected, is symmetric and the values are almost the same as in Figure 5.10 (a). The highest value of  $\sqrt{w'^2}/u_b$  was found near the wall, as expected. Near the wall the turbulence is highly anisotropic presenting different values for each component of the Reynolds Stress tensor trace (Silva Freire et al., 1998)

Unlike in the streamwise direction, the maximum value of the spanwise velocity fluctuation intensity was found at the narrow gap for the cases (e), (d) and (f), worthing  $\sqrt{w'^2}/u_b=0.25$ . As the position increases azimuthally, the magnitude of the intensities decreases until a minimum value,  $\sqrt{w'^2}/u_b \sim 0.08$  at  $90^\circ$ , after this position the value tends to increase again, but without recover its maximum value.

For the cases C, D and E, as the eccentricity increases the magnitude of the intensity  $\sqrt{w'^2}/u_b$  decreases until a value of  $\sqrt{w'^2}/u_b \sim 0.201$  for  $e=0.9$ . This decrease is expected after the analysis of the Figure 5.8 (f) where it was also possible to see a reduction in de velocity profile compared with the Figure 5.8 (e).

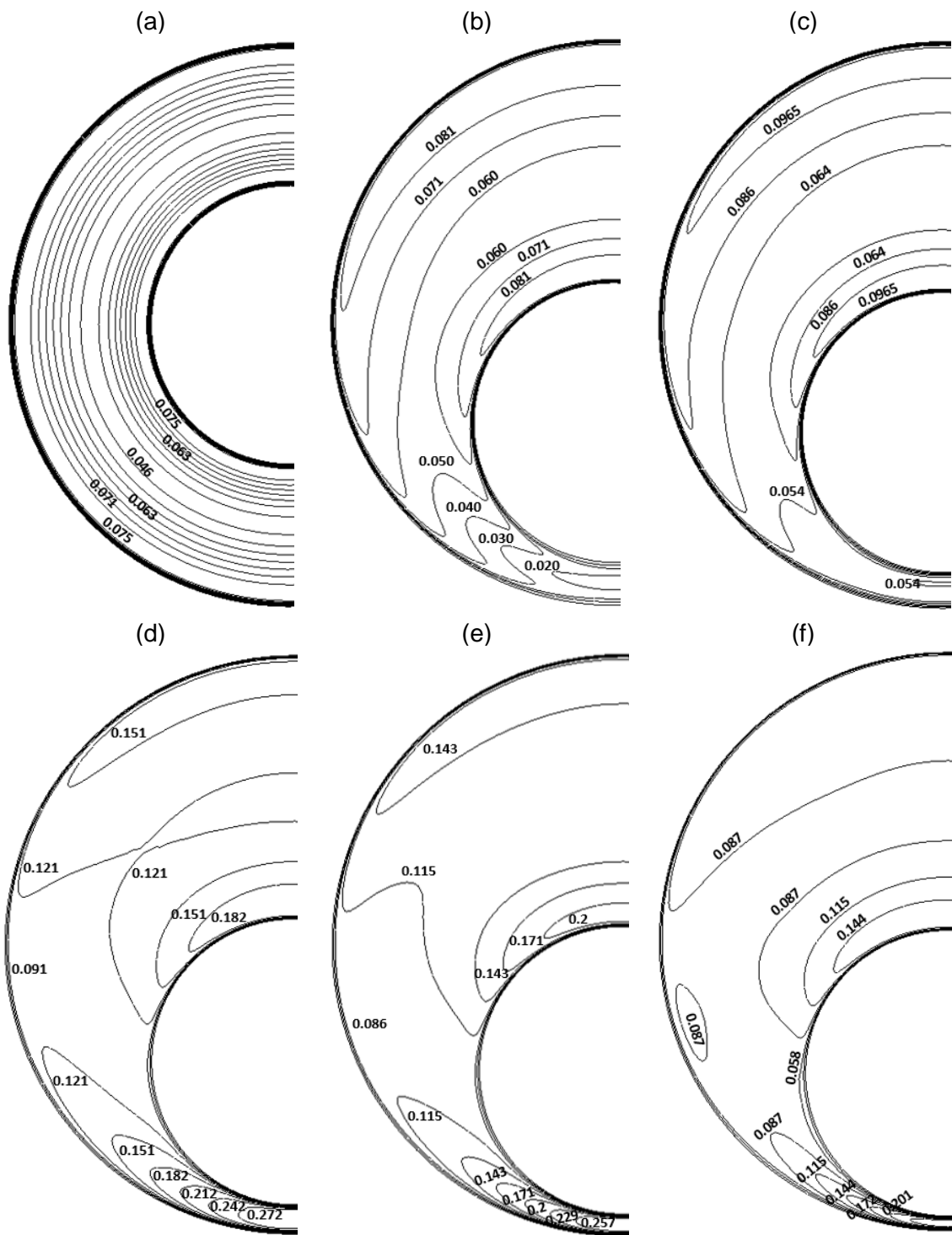


Figure 5.11 Spanwise velocity fluctuation intensity contours of  $\sqrt{w'^2}/u_b$  at  $x/D_h=50$ . (a) Reference Case. (b) Case A. (c) Case B. (d) Case C. (e) Case D. (f) Case E.

#### 5.2.4 The dynamics of the flow – the strouhal number for non-isothermal flow

As it was mentioned in section 5.1.2 the Strouhal number allows us to stress the frequencies in non-dimensional form. In order to achieve such goal macroscales of the problem are going to be used. The streamwise and spanwise velocity components time-traces were gathered for the cases C, D and E (corresponding to the eccentricities 0.8,0.85 and 0.9) for two streamwise positions along the channel, at  $x/D_h=30$  and  $x/D_h=50$ . The cases A and B were not studied because there were not velocity fluctuations. A Fast Fourier Transform FFT was applied in order to obtain the main frequency of the velocity time-traces and calculate the Strouhal number through the eq. 5.1.

Figure 5. presents the FFT performed at  $x/D_h=50$  for the cases C, D and E. Looking to the FFT of point 1, located at the narrow gap for the three cases the streamwise component has a frequency twice the spanwise component. As we move azimuthally the peaks of the dominant frequency are no longer as marked as at point 1. At point 3, in the streamwise component is still possible to identify a dominant frequency but in the spanwise component as the eccentricity increases, two dominating frequencies appear. Point 4 presents a similar behavior, but at this point the streamwise component is the one where there are two dominating frequencies.

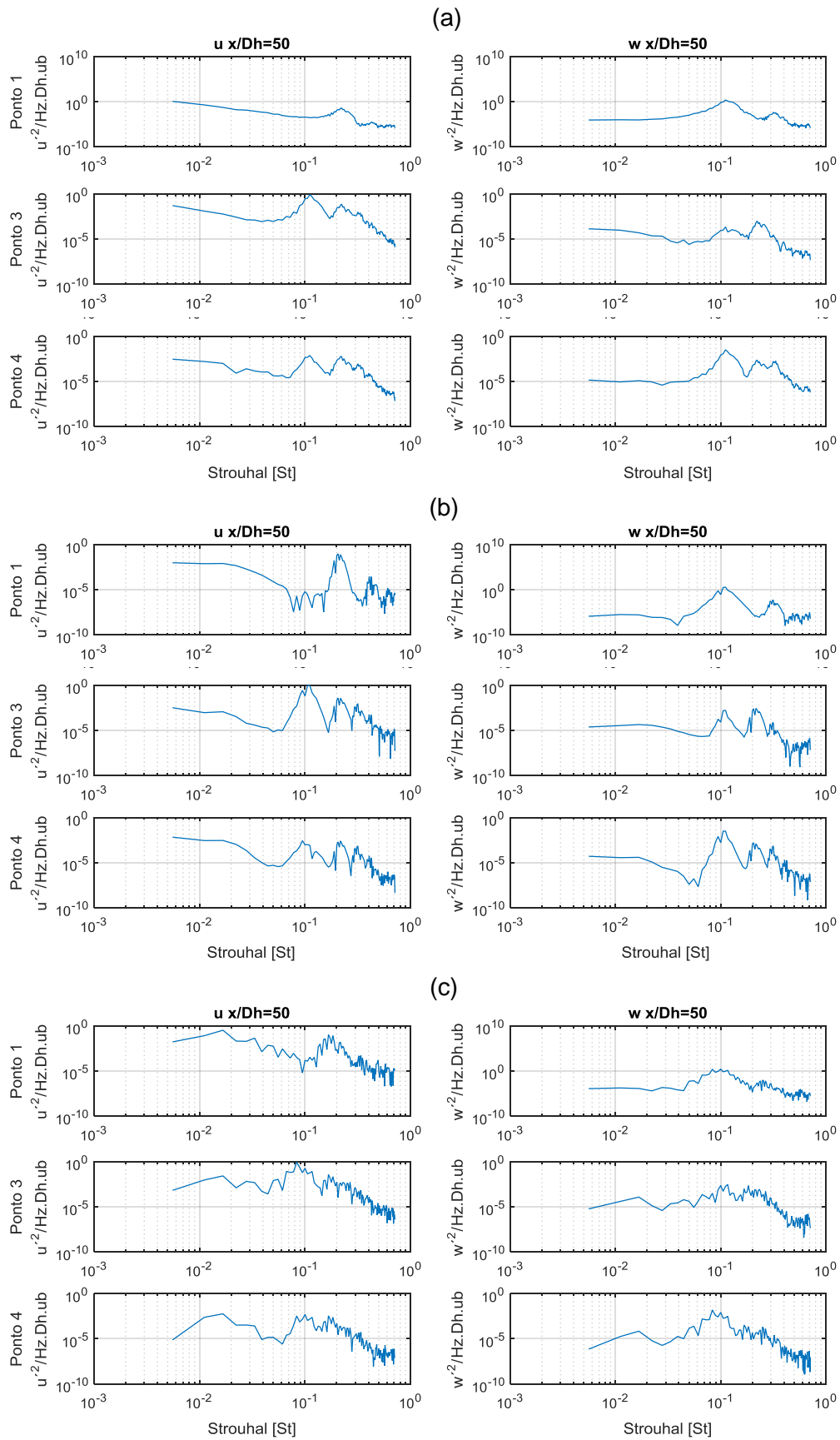


Figure 5.12 Fast Fourier Transform graphs at  $x/Dh=50$  (a) Eccentricity 0.8 (b) Eccentricity 0.85 (c) Eccentricity 0.9

Figure 5. presents the Strouhal number obtained for the cases and the positions previously indicated. The Strouhal number remains constant for all points investigated (1 and 5), located at the middle of the narrow gap and the wider gap respectively. Moreover, dimensionless frequency was found great agreement with the experimental work[1]. The frequency in the streamwise direction is twice compared with the spanwise direction, this particularity is in concordance with the experimental results of Choueri and Tavoularis[1].

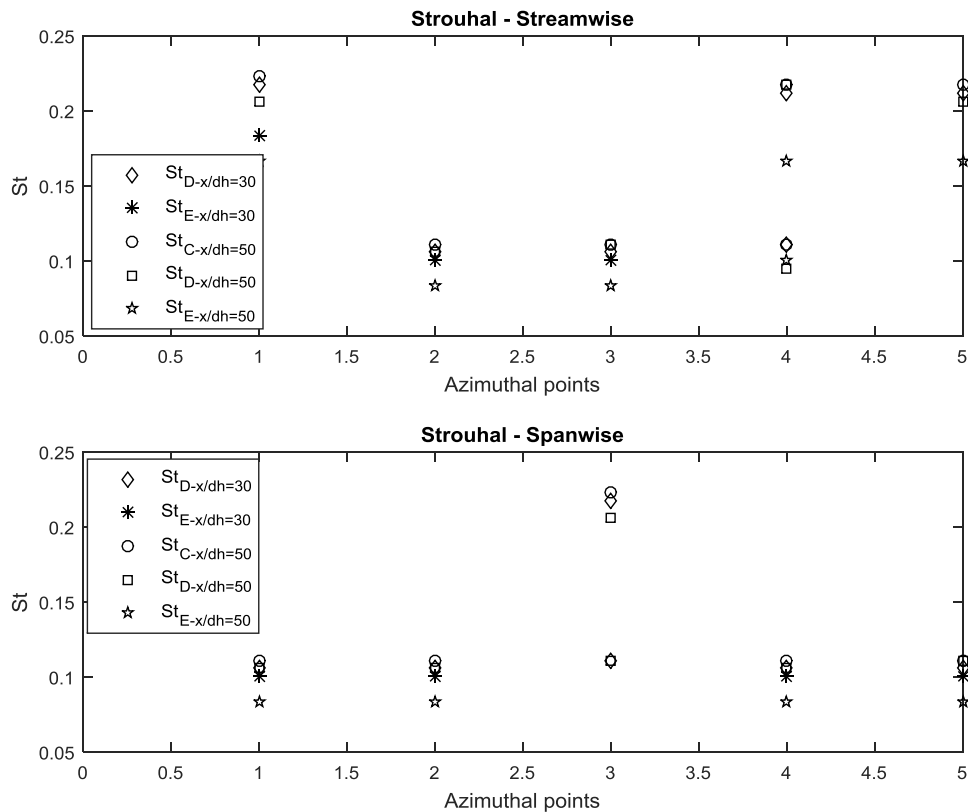


Figure 5.13 Strouhal number in the streamwise and spanwise directions at  $x/Dh=30$  and  $x/Dh=50$

### 5.2.5 The coherent structures visualization - q-criterion

The Q-criterion is the second invariant of the velocity gradient tensor [48]. IT represents the local balance between the vorticity magnitude and the shear strain rate. This criterion is applied in the domain and defines regions where the vorticity magnitude is greater than the magnitude of rate of strain, assigning the

regions where the vorticity, and, therefore, the coherent structures have evolved [49]. The equation (5.2) presents the expression used to obtain the Q-criterion,  $\omega$  is the instantaneous vorticity and  $S$  is also the instantaneous shear strain rate. The vorticity and the shear strain rate also can be seen as the antisymmetric and the symmetric component of the velocity gradient tensor [48].

$$Q = \frac{1}{2}(\omega^2 - S^2) \quad (5.2)$$

The Q-criterion must have a positive value in order to show the regions where the vorticity is more important than the shear strain. Figure 5.12 shows the isosurfaces of the Q-criterion along the channel colored by using the eddy viscosity for the concentric channel and the other five eccentricity cases, as well.

In the concentric case and the case A there is no coherent structures appearance. From the case B till the case E these structures start to appear always in pairs at each side of the narrow gap, after some distance from the inlet,  $x/D_h$ . It is also noticeable, in concordance with the previous figures, that as the eccentricity increases the gap instability onset is shortened and coherent structures are found closer to the inlet of the channel. In the case E, with the higher eccentricity, the coherent structures are present in almost all the length of the channel.

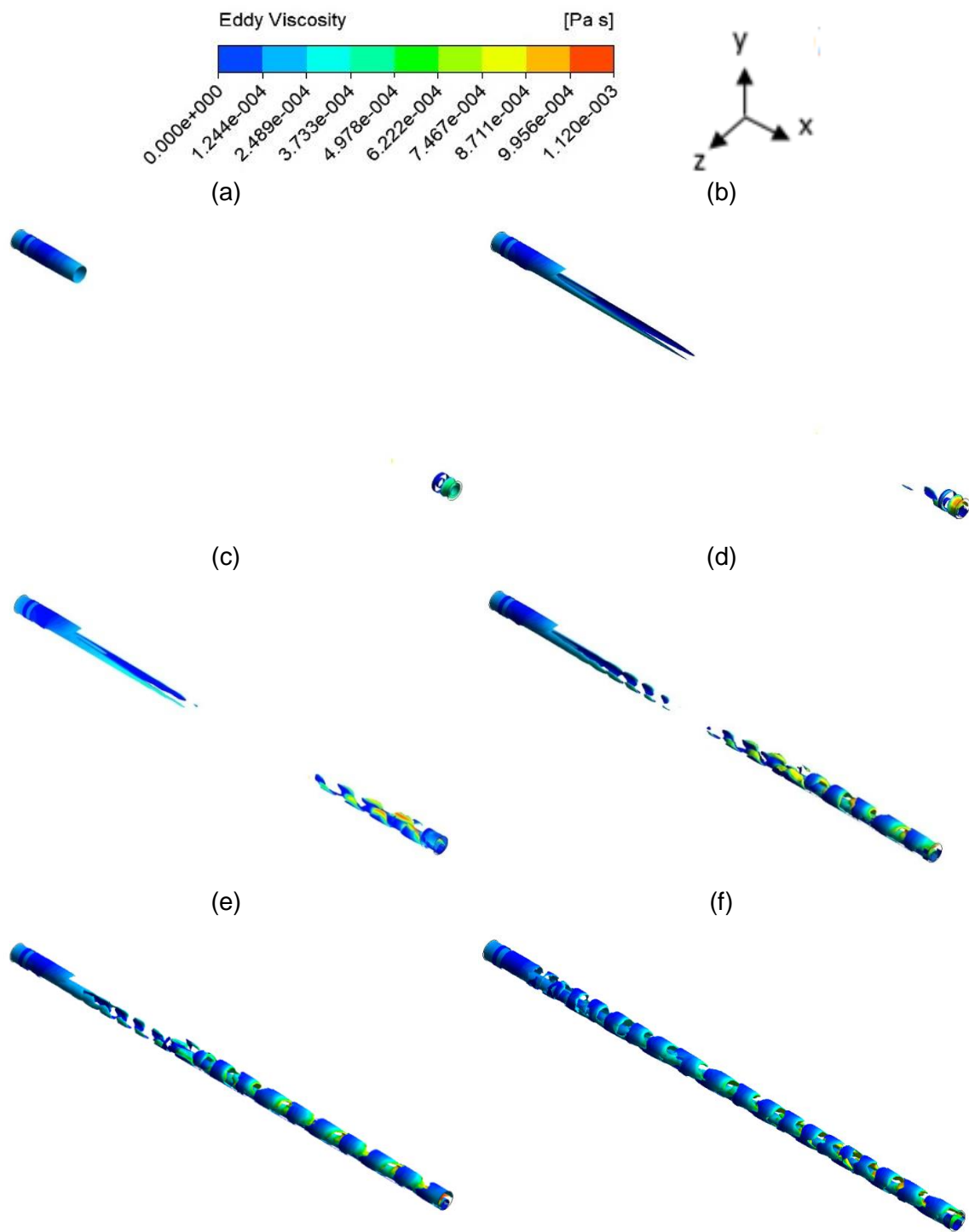


Figure 5.12 Flow visualization through the Q- criterion. (a) Reference case. (b) Case A. (c) Case B. (d) Case C. (e) Case D. (f) Case E.

### 5.3 Heat transfer – THE NUSSELT NUMBER AND THE ECCENTRICITY

#### 5.3.1 The Reference case

The heat transfer problem in the concentric case was numerically simulated and analyzed. The outcomes were faced against the analytic solution, through the equations presented in the section 3.3.2. In this case the equation (3.40) was applied to obtain the bulk temperature in the transversal plane. The heat transfer coefficient and the Nusselt number were computed through the equations (3.29) and (3.30), respectively. the simulated nusselt number was compared to the analytic equation 3.37.

The Figure 5.13 presents the variations of the surface temperature ( $T_s$ ) and bulk temperature ( $T_b$ ) in the reference case ( $e=0$ ). The surface temperature, is obtained for different stations along the inner rod, by averaging the temperatures as a function of the azimuthal position. By definition, the fully developed thermal condition for a channel with constant heat flux is achieved when the difference between the surface and bulk temperatures is constant in the streamwise direction [47]. Such behavior is shown in the Figure 5.13 below, roughly, at  $x/D_h = 20$  the thermal fully developed condition is achieved.

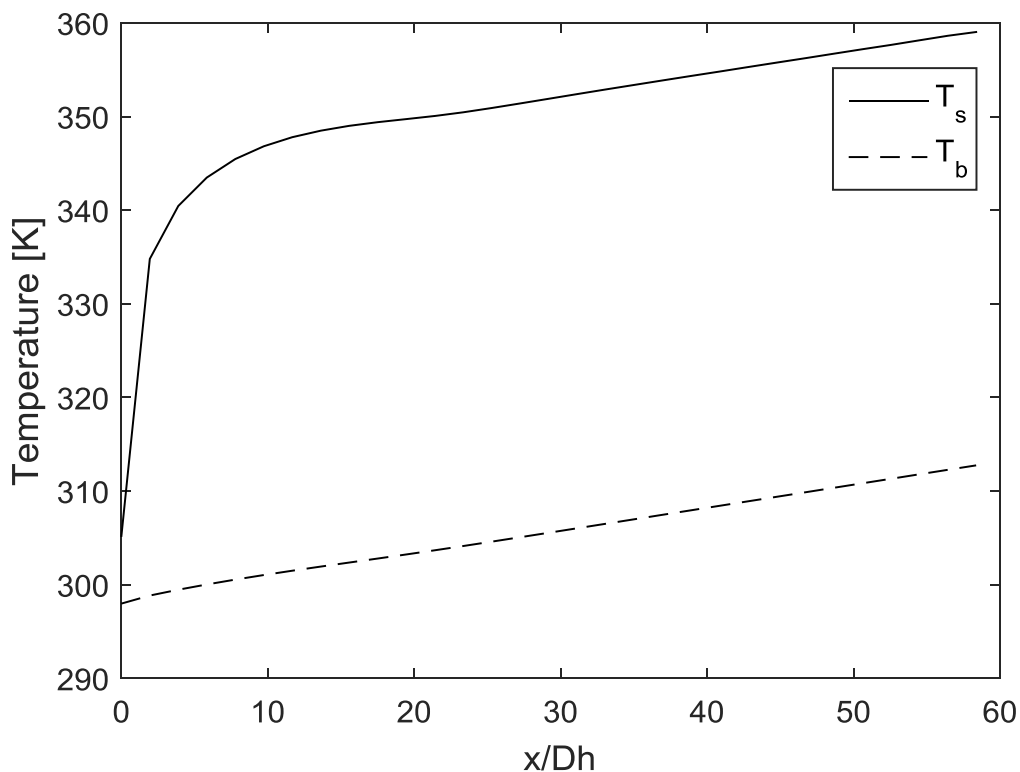


Figure 5.13 Axial temperature variations of the concentric case

The Table 5.2 presents the comparison between the Nusselt number obtained by applying the analytical equations and that one obtained from the numerical simulation. The Simulation under-predicted the Nusselt number in 12.43%, however, despite such difference, the model was thought to be able in predicting the non-isothermal problem. So, accepting the numerical computation as a valid result we also validate the mesh, thermal boundary conditions and turbulence model applied to solve the problem. It is important to notice that the result presented in the table below for the numerical simulation was taken in the transversal plane.

Table 5.2 Numerical and analytical results of the Nusselt number

	Nusselt number
Analytical equation (eq. 3.37)	49.65
Numerical Simulation	43.48

### 5.3.2 Eccentric channels

Taking into account that there is no any analytical solution to predict the nusselt number for the eccentric cases, the good accuracy of our previous simulation allows us to extend our numerical methodology to the new simulations. As mentioned in section 3.3.3, in order to obtain the surface temperature it was used the equation (3.40). The Figure 5.14 presents the comparison between the surface temperatures,  $T_s$ , for all the eccentric cases, along with the concentric case, used as a reference. The reference case is always depicted as a solid line.

As the eccentricity increases the temperature fluctuates with the flow field. The average temperature on the rod's surface starts to oscillate just few hydraulic diameter downstream from the inlet as the gap becomes tighter, it means, the eccentricity becomes higher. It is noticeable that the temperature difference between the reference case and the case B increases along the channel. When the velocity fluctuations starts to appear, at  $x/D_h=48$ , the surface temperature,  $T_s$ , decreases and reach a constant oscillation around a value near to the surface temperature obtained in the reference case, (A). Figure 5.14 shows the important role that the velocity fluctuation plays in the temperature

distribution. Furthermore, it shows how the velocity fluctuations are able to dissipate the high temperatures on the tube's surface.

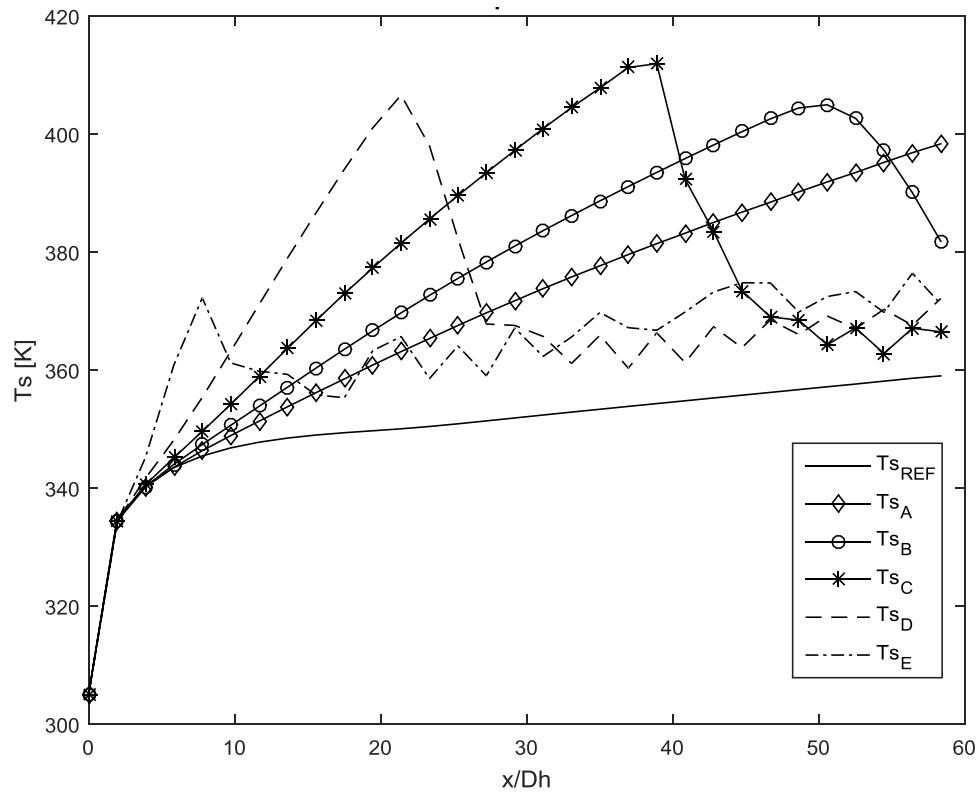


Figure 5.14 Surface temperature,  $T_S$ , along the channel for different eccentricities.

From the dynamical analysis, it was possible to see how the behavior of the flow changes when we move in the azimuthal direction. The fluctuation intensities for the streamwise direction, increases as we move from the narrow gap towards the wider gap as shown in Figure 5.15.

Figure 5.16 shows the Nusselt number for each simulated case as a function of the azimuthal direction. The position  $0^\circ$  is located in the narrow gap and  $180^\circ$  the wider gap (clockwise). The Nusselt number was obtained using the equations (3.29) and (3.30). The calculations were made using the bulk temperature at  $x/D_h=50$ . The local surface temperature, as a function of the angular position on the inner tube, was taken each  $10^\circ$ .

For the concentric case it is possible to see that the Nusselt number has a constant behavior. For the two first eccentricity cases (cases A and B) the Nusselt number is considerably reduced at  $0^\circ$  taking a value of around 23%

compared with the reference case (case A,  $e=0$ ). This values can be explained taking into account that in this positions the area, and therefore the velocity, is lower. Since the average Nusselt number is ruled by the Prandtl and Reynolds numbers, local Nusselt is ruled by local scales. In the narrow gap the viscous effects are greater and, therefore, the local velocity and Reynolds are diminished, affecting, in negative way, the local heat convection. Another striking features of the flow at such positions is the absence of the flow instabilities. As the angle is increasing, the local Nusselt number starts to increase until a its maximum value of approximately 60 at  $180^\circ$ , taking at  $90^\circ$  the same value obtained in the concentric case.

It is remarkable to observe distinguished Nusselt number distribution for higher eccentricities. In the case D ( $e=0.85$ ) the values are quite similar to the ones obtained in the reference case, despite the obvious reduction in the streamwise velocity at the narrow gap showed in the Figure 5.7. This may be explained by the intensity of the velocity fluctuations presented in Figure 5.10 and Figure 5.11. From these figures it is possible to observe that in the narrow gap, where the streamwise velocity is affected by the area reduction and viscous effects, the flow fluctuation produced in the spanwise direction attenuates the effects of the velocity reduction and is strong enough to maintain the Nusselt number about only 10% lower with respect to the reference case.

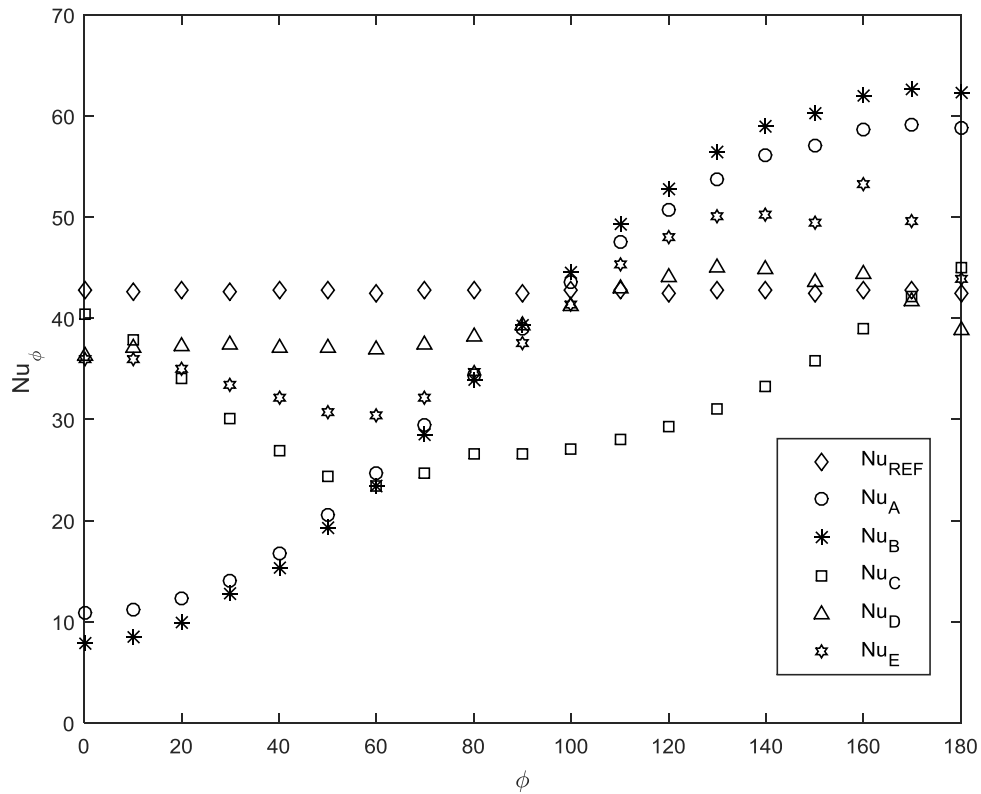


Figure 5.16 Nusselt number distribution as a function of azimuthal position.

To confirm the influence of the velocity fluctuations in the heat transfer process, Nusselt distribution around the inner tube was gathered at two different streamwise stations,  $x/D_h=10$  and  $x/D_h=50$ , for two different cases, D and E. It is important to highlight that at  $x/D_h=10$  the case D ( $e=0.85$ ) does not have velocity fluctuations. In the case E ( $e=0.9$ ), at  $x/D_h=10$  is the point of the onset of the velocity fluctuations, but they are just beginning and have not reached a stable behavior.

Figure 5.17 shows the Nusselt number distribution at  $x/D_h=10$  for the cases D and E ( $e=0.85$  and  $0.9$  respectively). The local Nusselt data were stressed as a ratio its local value and the concentric Nusselt. It is interesting to observe that the Nusselt decreasing from zero up to  $20^\circ$ , starting to increase again, reaching its maximum at about  $60^\circ$ . As the azimuthal position increases the local velocity also increases and the gap size becomes wider. After approximately  $100^\circ$ , the Nusselt distribution is found almost constant, being the values comparable with the reference case. For farther stations from the channel's inlet, at  $x/D_h=50$ , both cases have developed velocity fluctuations. Even though, at the narrow gap vicinity ( $0^\circ$  up to  $60^\circ$ ) the Nusselt number is

reduced, in comparison with the reference case ( $e=0$ ), its lowest value is about 70% of the value obtained for the concentric case and takes place at  $60^\circ$ .

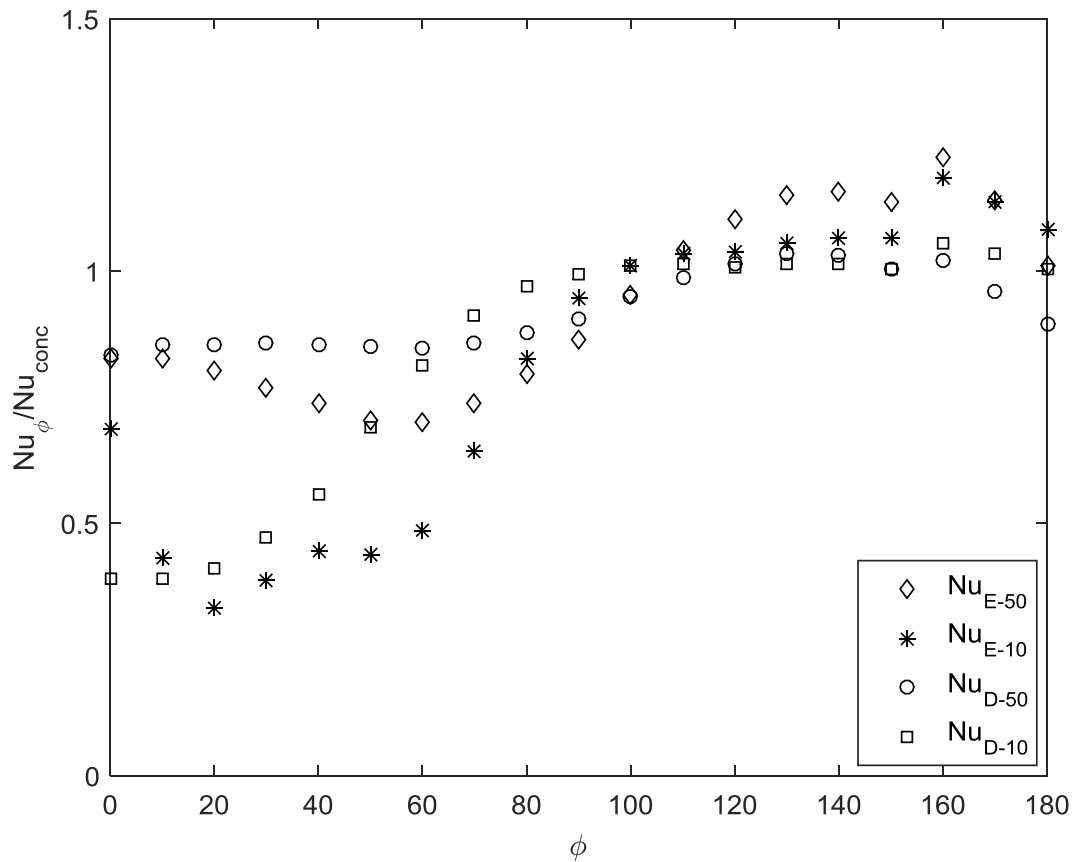


Figure 5.17 Variation of the Nusselt number in the azimuthal direction for the cases D and E at two different positions along the channel  $x/D_h=10$  and  $x/D_h=50$ .

It is important to emphasize that it seems to have an optimal value of the eccentricity in order to compensate the effects of the tight gap and maintain the values of the Nusselt number similar with the concentric case. For eccentricities with values lower and higher than 0.85, it seems that the flow does not develop a dynamical behavior enough to maintain the Nusselt number sufficiently similar to the reference case.

## 6 CONCLUSIONS

The aim of the present work was to analyze the mean average flow quantities and the dynamics of the developing turbulent flow in eccentric channels. We also furthered our research by investigating the influence of the velocity fluctuations on the convective heat transfer coefficient on the tube's surface, through the coupling problem, turbulence associated to the heat transfer. The onset gap instability and its dependence on the eccentricity was also target of our investigation.

In order to achieve this goal it was first performed a incompressible three dimensional unsteady flow simulation to predict the main features of the turbulent flow in a compound channel which contains a narrow gap. The computational domain is the same one which Choueiri and Tavoularis [1] whose the authors carried out their experimental campaign. The channel was composed by two different pipes with  $d/d = 0.50$ , being the inner one displaced from the center of the cross-sectional plane, forming an annular narrow passage. The Reynolds number based on the hydraulic diameter ( $D_h$ ) and the bulk velocity ( $u_b$ ) and the kinematic viscosity,  $\nu$ , yielding  $Re = 7300$ . The computations were performed in a finite volume commercial software applying an anisotropic hybrid URANS/LES model known as DES-SST to overcome the additional diffusivity caused by the turbulence.

From the comparison of the first simulation with the experimental results it was possible to verify three different regions in the flow developing processes along the channel. moreover, the turbulence model successfully predicted the main characteristics reported by the experimental work performed by Choueri and Tavoularis [1]. Regardless the azimuthal region, were the flow is located, the entrance region (ER), the fluctuation growth (FG) and the rapid mixing (RM) regions could be observed in the five points of analysis.

The Strouhal number was analyzed in the streamwise and spanwise directions. It was found that it reaches an almost constant value at the end to the FG region. This agrees with the point where the velocity fluctuations begins and also the mean velocity reach its stable value. The Strouhal number in the streamwise direction is almost twice than the spanwise direction. This results also matches with the experimental work of Choueiri and Tavoularis [1].

A second set of simulation was performed increasing the Reynolds number to 15000 and adding thermal boundary conditions to the problem. The eccentricity was ranged from 0.7 to 0.9 in intervals of 0.05. The heat flux applied was 2000 [W/m<sup>2</sup>] at the inner wall. The outer wall was kept isolated. The fluid properties were also kept unchangeable, so, the Prandtl number was set 0.70 throughout the computations.

The intensities of the velocity fluctuations were studied for the streamwise and spanwise components. With this analysis was possible to observe that in the narrow gap the spanwise velocity has a more important intensity compared with the streamwise velocity. This leads to think that exist a secondary flow produced by the coherent structures that are crossing through the gap. As we move azimuthally the intensities in the spanwise direction decrease and the intensities in the streamwise direction increases until a maximum value around 90°.

The Strouhal number was again analyzed to observe if adding the heat transfer problem caused some effect in the dynamics of the flow. The values of the Strouhal number in the narrow gap remained constant and in concordance with the work of Choueiri and Tavoularis [1]. In the azimuthal direction, at positions 3 and 4, the flow presented two dominating frequencies for the spanwise direction for the point 3 and in the streamwise direction for the point 4. At point 2, the frequency in the streamwise and spanwise direction is the same and point 5 presented the same behavior as point 1 with the frequency in the streamwise direction twice than the spanwise direction.

The concentric case was studied in order to validate the methodology implemented for the heat transfer problem by making a comparison with the analytical equations given by Gnielinski [11]. The Nusselt number predicted by the code was about 12% lower than that computed from analytic equations.

As the eccentricity increases it is evident that the onset of the velocity fluctuations is shortened for both streamwise and spanwise directions. Analyzing the velocity profiles it was evident how the velocity fluctuations played an important role in order to ate the gap vicinity as the eccentricity increases. At the streamwise station where the fluctuations appeared for the first time the velocity profiles presented higher values in comparisson to the locations where the fluctuations were not observed.

The surface temperature of the inner rod was also seen affected by the velocity fluctuations. The fluctuating flow field led the mean average temperature to a sudden decrease that takes place at the very same point of the onset of the velocity fluctuations. Affected by the velocity fluctuation the mean average surface temperature oscillates around a value near to the one obtained for the concentric case and the onset of these fluctuations is earlier as the eccentricity increases.

The Nusselt number distribution on the inner rod's surface was computed for all cases. Due to the flow symmetry in the concentric case, there was no variation of the Nusselt number, however, it was used as a reference case. But for the cases with higher eccentricities, it was really interesting to notice that even when the velocity and fluctuation intensities in the streamwise directions were considerably reduced at the narrow gap, the Nusselt number was comparable with the concentric case. This was found to be consequence of the high velocity fluctuation intensities in the spanwise direction at the narrow gap vicinity. So, the result lead to conclude that the spanwise velocity fluctuation seems to play an important role in the heat transfer process.

Besides, for the case with an eccentricity of 0.85 the values of the Nusselt number were closer to the concentric case than those ones found in the pipes with eccentricity 0.8 and 0.9. This allows to think that there is an optimal value in which the velocity fluctuations intensities affect the flow in a way that are able to attenuate the effect of the velocity reduction in the narrow gap maintaining the Nusselt number comparable to the one found for the concentric case.

## **6.1 Future works**

The influence of the heat flux and Reynolds number has not been validated, that is why for future works we recommend:

- Analyze different heat fluxes and Reynolds numbers in a longer channel in order to study the delay in the velocity fluctuations as a function of the Reynolds number.
- Analyze if for other thermal and dynamical conditions there is a change in the best eccentricity case obtained in the present work.

- Validate the fluctuation intensities in the three components in lower intervals and for different dynamical conditions.

## 7 REFERENCES

1. CHOUEIRI, G.; TAVOULARIS, S. Experimental investigation of flow development and gap v vortex street in an eccentric annular channel. Part 1. Overview of the flow structure. **J. Fluid Mech**, v. 752, p. 521-542, 2014.
2. GOULART, J.; WISSINK, J.; WROBEL, L. Numerical simulation of turbulent flow in a channel containing a small slot. **International Journal of Heat and Fluid Flow** , v. 61, p. 343-354, 2016.
3. DOUGLAS, J. **Turbulent flow in concentric and eccentric annuli**. University of British Columbia. [S.I.]. 1963.
4. DREISSLER, R.; TAYLOR , M. **Analysis of fully developed turbulent heat transfer and flow in annulus with various eccentricities**. National advisory committee for aeronautics. [S.I.]. 1955.
5. USUI, H.; TSURUTA, K. Analysis of fully developed turbulent flow in na eccentric annulus. **Journal of chemical engineering of Japan**, v. 13, p. 445-450, 1980.
6. LEE, Y.; BARROW, H. Turbulent flow and heat transfer in concentric and eccentric annuli. **Proc Instn Mech Engrs**, v. 178, p. 1-16, 1963.
7. NOURI, J.; UMUR, H.; WHITELAW, H. Flow of newtonian and non-newtonian fluids in concentric and eccentric annuli. **Journal of fluid mechanics**, v. 253, p. 617-641, 1993.
8. NIKITIN, N.; WANG, H.; CHERNYSHENKO, S. Turbulent flow and heat transfer in eccentric annulus. **J. Fluid Mech**, v. 638, p. 95-116, 2009.
9. CARLSON, L.; IRVINE, T. Fully developed pressure drop in triangular shaped ducts. **J. Heat transfer, Trans. Amer. SOC. Mech. Engrs**, v. 441, 1961.
10. REYNOLDS, W.; LUNDBERG, R.; MCCUEN, P. Heat transfer in annular passages. **Int J Heat Mass Trans**, v. 6, p. 483-529, 1963.
11. GNIELINSKI, V. Heat transfer coefficients for turbulent flow in concentric annular ducts. **Heat transfer engineering**, v. 30, p. 431-436, 2009.
12. KAYS, W.; LEUNG, E. Heat transfer in annular pasagges-hydrodynamically developed turbulent flow with arbitrary prescribed heat flux. **Int. J. Heat Mass Transf.**, v. 6, p. 635-640, 1978.
13. JUDD, R.; WADE, J. Forced convection heat transfer in eccentric annular passages. **Heat transfer and fluids mechanics Institute** , p. 272-288,

1963.

14. OGINO, F.; SAKANO, T.; MIZUSHINA, T. Momentum and heat transfers from fully developed turbulent flow in eccentric annulus to inner and outer tube walls. **Warme und Stoffubertragung**, v. 21, p. 87-93, 1987.
15. REDBERG, P.; CHARLES, M. Axial laminar flow in a circular pipe containing a fixed eccentric core. **The Canadian Journal of Chemical Engineering**, p. 148-151, August 1962.
16. SNYDER, W.; GOLDSTEIN, G. An analysis of fully developed laminar flow in an eccentric annulus. **AIChE Journal**, v. 11, p. 462-467, May 1965.
17. PIOT, E.; TAVOULARIS, S. Gap instability of laminar flows in eccentric annular channels.
18. QUARMBY, A. An experimental study of turbulent flow through concentric annuli. **Int. J. Mech. Sci.**, v. 9, p. 206-221, 1967.
19. CLUMP, C.; KWASNOSKI, D. turbulent flow in concentric annuli. **AIChE Journal**, v. 14, p. 164-168, January 1968.
20. LAWN, C.; ELLIOT, J. Fully developed turbulent flow through concentric annuli. **Journal Mechanical Engineering Science** , v. 14, p. 195-204, 1972.
21. REHME, K. Turbulent flow in smooth concentric annuli with small radius ratio. **J. Fluid Mech.**, v. 64, p. 263-287, 1974.
22. SPEZIALE, C.; ABID, R.; ANDERSON, E. Critical evaluation of two-equation models for near-wall turbulence. **AIAA Journal**, v. 30, p. 324-331, February 1992.
23. AZOUZ, I. et al. **Numerical simulation of turbulent flow in concentric and eccentric annuli**. Fluid Dynamics Conference. Orlando: [s.n.]. 1993. p. 1-11.
24. CHUNG, S.; HOON RHEE, G.; JIN SUNG, H. Direct simulation of turbulent concentric annular pipe flow Part 1: Flow field. **International Journal of Heat and Fluid Flow**, v. 23, p. 426-440, 2002.
25. DOU, H.; KHOO, B.; TSAI, H. Determining the critical condition for turbulent transition in a fully-developed annulus flow. **Journal of Petroleum Science and Engineering**, v. 73, p. 41-47, 2010.

26. CAJARILESCOV, P.; TODREAS, N. Experimental and analytical study of axial turbulent flows in an interior subchannel of a bare rod bundle. **Journal of Heat transfer**, p. 262-268, May 1976.
27. BAE, J. H.; PARK, J. H. Analytical prediction of turbulent friction factor for a rod bundle. **Annals of Nuclear Energy**, v. 38, p. 348-357, 2011.
28. BERTOCCHI, F.; ROHDE, M.; KLOOSTERMAN, J. L. LDA measurements of coherent flow structures and cross-flow across the gap of a compound channel with two half-rods. **Nuclear Engineering and Design**, v. 326, p. 17-30, 2018.
29. LAKEHAL, D. Highly-resolved LES of turbulent convective flow along a PWR rod bundle. **International Journal of Heat and Mass Transfer**, v. 122, p. 785-794, 2018.
30. LEE, Y.; BARROW, H. Turbulent flow and heat transfer in concentric and eccentric annuli. **Proc Instn Mech Engrs**, v. 178, p. 1-16, 1963.
31. CHENG, K.; HWANG, G. Laminar forced convection in Eccentric annuli. **AIChE Journal**, p. 510-512, May 1968.
32. WILSON, N.; MEDWELL, J. An analysis of heat transfer for fully developed turbulent flow in concentric annuli. **Journal of Heat Transfer**, p. 43-50, February 1968.
33. QUARMBY, A.; ANAND, R. Turbulent heat transfer in the thermal entrance region of concentric annuli with uniform wall heat flux. **Int. J. Heat Mass Transfer**, v. 13, p. 395-411, 1970.
34. DAWOOD, H. et al. Forced, natural and mixed-convection heat transfer and fluid flow in annulus: A review. **International Communications in Heat and Mass Transfer**, p. 1-13, 2015.
35. CHUNG, S.; JIN SUNG, H. Direct numerical simulation of turbulent concentric annular pipe flow Part 2: Heat transfer. **International Journal of Heat and Fluid Flow**, v. 24, p. 399-411, 2003.
36. SU, J.; SILVA, A. Analytical prediction of friction factors and Nusselt numbers of turbulent forced convection in rod bundles with smooth and rough surfaces. **Nuclear Engineering and Design**, v. 217, p. 111-127, 2002.
37. CHANG, D.; TAVOULARIS, S. Simulations of turbulence, heat transfer and mixing across narrow gaps between rod-bundle subchannel. **Nuclear**

- Engineering and Design**, v. 238, p. 109-123, 2008.
38. DUAN, Y.; HE, S. Heat transfer of a buoyancy-aided turbulent flow in a trapezoidal annulus. **International Journal of Heat and Mass Transfer**, v. 114, p. 211-224, 2017.
  39. SILVA, A. **Introdução à Turbulência**. Universidade Federal do Rio de Janeiro. [S.l.], p. 54.
  40. REYNOLDS, O. On the dynamical theory of incompressible viscous fluids and the determination of the criterion. **Philosophical Transactions of the Royal Society of London**, v. 186, p. 123, 1895.
  41. SILVA, A.; MENUT, P.; SU, J. **Turbulência**. Rio de Janeiro: Associação Brasileira de Ciências Mecânicas, v. I, 2002.
  42. MENTER, F. Two-Equation eddy-viscosity turbulence models for engineering applications. **AIAA Journal**, v. 23, p. 1598-1605, 1994.
  43. ANSYS, INC. **ANSYS CFX-Solver Modeling Guide**. 14. ed. Canonsburg: [s.n.], 2011.
  44. SMAGORINSKY, J. General Circulation Experiments with the Primitive Equations. **Monthly Weather Review**, n. 91, p. 99-164, March 1963.
  45. STRELETS, M. **Detached eddy simulation of massively separated flows**. 39th Aerospace sciences meeting and exhibit. [S.l.]: [s.n.]. 2001.
  46. ÇENGEL, Y. Heat Transfer: A practical approach. In: ÇENGEL, Y. **Heat Transfer: A practical approach**. 2a. ed. [S.l.]: McGraw-Hill, 2003. Cap. 7, p. 932.
  47. INCROPERA, F. **Fundamentals of heat and mass transfer**. 6th. ed. New Jersey: John Wiley & Sons.
  48. DUBIEF, Y.; DELCAYRE, F. On coherent-vortex identification in turbulence. **Journal of turbulence**, v. 11, p. 23, 2000.
  49. HOLMÉN, V. **Methods for vortex identification**. [S.l.], p. 46. 2012.
  50. BERTOCCHI, F.; ROHDE, M.; KLOOSTERMAN, J. L. LDA measurements of coherent flow structures and cross-flow across the gap. **Nuclear Engineering and Design**, v. 326, p. 17-30, 2018.
  51. SHIIBARA, N.; NAKAMURA, H.; YAMADA, S. Unsteady characteristics of turbulent heat transfer in a circular pipe upon sudden acceleration and

deceleration of flow. **International Journal of Heat and Mass Transfer**, v. 113, p. 490-501, October 2017.

52. NARASIMHAN, A.; LAGE, J.; NIELD, D. New theory for forced convection through porous media by fluids with temperature-dependent viscosity. **Journal of Heat Transfer**, v. 123, p. 1045-1051, 2001.
53. MÖLLER, S. On phenomena of turbulent flow through rod bundles. **Experimental Thermal and Fluid Science**, v. 4, p. 25-35, 1991.
54. BEJAN, A. **Convection Heat Transfer**. 3th. ed. New Delhi: John Wiley & Sons, 2004.
55. WILCOX, D. **Turbulence model for CFD**. 2nd. ed. California: DCW Industries, 2000.